Chromatin remodeling with combined FACT and BET inhibition disrupts oncogenic transcription in Diffuse Midline Glioma

Authors:

Holly Holliday[1,2]*, Aaminah Khan[1,2]*, Anahid Ehteda[1,2], Samuel E. Ross[3], Nisitha Jayatilleke[1], Anjana Gopalakrishnan[1], Xinyi Guo[1], Jie Liu[1], Hieu Nguyen[1], Alvin Lee[1], Yolanda Colino Sanguino[1,2], Marcel E. Dinger[3], Chelsea Mayoh[1,2], Benjamin S. Rayner[1,2], Maria Tsoli[1,2]**, David S. Ziegler[1, 2, 4]**

* ** equal contribution

Affiliations:

1. Children's Cancer Institute, Lowy Cancer Research Centre, UNSW Sydney, Sydney, NSW, Australia
2. School of Clinical Medicine, UNSW Sydney, Sydney, NSW, Australia
3. School of Life and Environmental Sciences, University of Sydney
4. Kid's Cancer Centre, Sydney Children's Hospital, Randwick, NSW, Australia

Keywords: FACT; BRD4; BET proteins; Diffuse Midline Glioma; DMG; DIPG; H3K27M; Epigenetics; Chromatin; Histones; CBL0137; JQ1; BET inhibitors; Epigenetic therapies; Pre-clinical

Running title: BETing on FACT in DMG

Corresponding authors: Professor David S. Ziegler, Kids Cancer Centre, Sydney Children's Hospital, High St, Randwick 2031 Australia, +61 (02) 9382 1730, d.ziegler@unsw.edu.au

Declaration of Interest statement: DSZ declares consulting/advisory board fees from Bayer, Astra Zeneca, Accendatech, Novartis, Day One, FivePhusion, Amgen, Alexion, and Norgine and research support from Accendatech. The remaining authors have declared that no competing interests exist.

Abstract

Aberrant epigenetic regulation is a hallmark of Diffuse Midline Glioma (DMG), an incurable pediatric brain tumor. The H3K27M driver histone mutation leads to transcriptional dysregulation, indicating that targeting the epigenome and transcription may be key therapeutic strategies against this highly aggressive cancer. One such target is the Facilitates Chromatin Transcription (FACT) histone chaperone. We found FACT to be enriched at developmental gene promoters, coinciding with regions of open chromatin and binding motifs of core DMG regulatory transcription factors. Furthermore, FACT interacted and co-localized with the Bromodomain and Extra-Terminal Domain (BET) protein BRD4 at promoters and enhancers, suggesting functional cooperation between FACT and BRD4 in DMG. *In vitro*, a combinatorial therapeutic approach using the FACT inhibitor CBL0137, coupled with BET inhibition revealed potent and synergistic cytotoxicity across a range of DMG cultures, with H3K27M-mutant cells demonstrating heightened sensitivity. These results were recapitulated *in vivo*, significantly extending survival in three independent orthotopic PDX models of DMG. Mechanistically, we show that CBL0137 treatment decreased chromatin accessibility, synergizing with BET inhibition to disrupt transcription, silencing several key oncogenes including *MYC, PDGFRA* and *MDM4*, as well as causing alterations to the splicing landscape. Combined, these data highlight the therapeutic promise of simultaneously targeting FACT and BRD4 in DMG, proposing a novel strategy for combating this devastating pediatric brain tumor.

Introduction

Diffuse midline glioma (DMG) is a highly aggressive brain tumor predominantly diagnosed in children under 10 years old. Recently classified as 'DMG K27-altered' by the 2021 World Health Organization, this designation recognizes the characteristic epigenetic dysregulation that arises from either the recurrent lysine-to-methionine driver mutations in Histone H3.1 and H3.3 genes (H3K27M), or overexpression of the oncohistone mimic EZHIP [1-7]. Both H3K27M and EZHIP inhibit Polycomb Repressive Complex 2 (PRC2) activity, resulting in a drastic reduction of Histone H3K27 trimethylation (H3K27me3), increased H3K27 acetylation (H3K27ac) and DNA hypomethylation. This culminates in an aberrant epigenetic landscape permissive to heightened transcriptional activity [8-14].

While direct therapeutic targeting of H3K27M has not been possible, targeting of epigenetic and transcription regulators has shown promise in several pre-clinical models of DMG (reviewed in [15, 16]). Among these regulators, the histone chaperone Facilitates Chromatin Transcription (FACT) comprising of two protein subunits; SSRP1 and SPT16, has garnered attention [17-19]. FACT plays a pivotal role in maintaining chromatin integrity by facilitating nucleosome turnover during transcription, DNA replication and repair. This chaperone is abundantly expressed in cancer cells, making it an attractive therapeutic target [20, 21].

The curaxin compound CBL0137 indirectly inhibits FACT by intercalating with DNA and trapping FACT on chromatin (c-trapping), effectively depleting the functional pool of this important chaperone [22-24]. We and others have demonstrated CBL0137 to be active against multiple tumor types, including neuroblastoma, glioblastoma, medulloblastoma, and diffuse intrinsic pontine glioma (DIPG)/DMG [19, 25-29]. This growing body of preclinical work has led to the advancement of CBL0137 to a Phase I/II clinical trial for pediatric patients with solid tumors, including DMG (NCT04870944). However, the aggressive nature of DMG necessitates combination therapies to address therapeutic resistance and reduce effective therapeutic doses. While initial studies combining CBL0137 with the pan-HDAC inhibitor panobinostat has shown promise against DMG pre-clinically [19], concerns over panobinostat's high toxicity, and limited efficacy, led to its withdrawal from clinical studies and highlights the need for alternative drug combinations [30].

Disruption of transcription has proven effective against many 'transcription addicted' malignancies, often achieved by targeting Bromodomain and Extra-Terminal Domain (BET) proteins such as BRD4 [31]. BRD4 recruits the transcriptional machinery to hyper-acetylated

chromatin at super-enhancers [32, 33], making it an attractive target against DMG, as demonstrated in the preclinical setting ([34-39] and reviewed in [40]). JQ1, among other BET inhibitors, has demonstrated pronounced efficacy in DMG, through transcriptional disruption leading to cytostatis [35]. Subsequently, the clinically relevant BET inhibitor trotabresib (CC-90010) has progressed to clinical trials for adults and children with brain cancer (NCT04047303, NCT04324840, NCT03936465). However, modest anti-tumor activity observed in adult monotherapy BET inhibitor trials necessitates the identification of synergistic combinations [40].

Here we describe the promising efficacy of FACT and BET inhibition as an epigenetic combination treatment in cell line and animal models of DMG. Mechanistically, this epigenetic intervention induces changes to chromatin structure and transcriptional profiles. Moreover, FACT inhibition with CBL0137 leads to chromatin closure at gene promoters, which when combined with BET inhibition, results in widespread changes to the transcriptome. Several key oncogenes vital for DMG growth, such as *MYC, PDGFRA,* and *MDM4* are directly regulated by FACT and BRD4, and effectively silenced by dual inhibition of these targets. These findings suggest a new strategy for inhibiting multiple oncogenic and otherwise 'untargetable' pathways in DMG.

Results

FACT and BRD4 are overexpressed, interact, and co-localize at active regulatory elements in DMG

Our earlier work identified FACT inhibition with CBL0137 to be a promising epigenetic therapy against DMG [19]. In order to further elucidate the genes bound and potentially regulated by FACT, and its established interaction with the H3K27M oncohistone [19, 41], we sought to map the genome-wide binding sites of the FACT subunit SPT16 in H3.3K27M-mutant HSJD-DIPG007 cells using Cleavage Under Targets and Release Using Nuclease (CUT&RUN). We identified 1,095 SPT16 peaks common to two independent replicates, which were over-enriched at promoters of genes involved in migration, morphogenesis, and development (FDR < 0.05) (**Fig 1A-B and Table S1A**). Furthermore, motifs for developmental and epithelial-to-mesenchymal transition (EMT) transcription factors (TFs) were enriched at SPT16 binding sites, including master regulators of DMG and oligodendrocyte development TCF12 (p = 4.819e-14) and OLIG2 (p = 4.281e-9) [42, 43], and SNAI1 (p = 3.58e-8), which is known to promote an invasive phenotype in malignant

gliomas [44, 45] (**Fig 1C**). This indicates that FACT facilitates transcription driven by these critical transcription factors.

We next analyzed SPT16 occupancy at different regulatory elements and separately determined the accessibility of these regions using Assay for Transposase-Accessible Chromatin using sequencing (ATAC-seq). H3K27M and H3K27ac are known to incorporate into heterotypic H3K27M-H3K27ac nucleosomes, which are bound by acetyl-binding BET proteins at enhancer elements [36, 46], prompting us to analyze FACT colocalization with these nucleosomes. Interestingly, SPT16, H3K27M and BRD4, were enriched at accessible transcription start sites (TSSs), promoters marked by H3K4me3, and enhancers marked by H3K27ac. Conversely, these proteins were absent from inaccessible H3K27me3-marked heterochromatin (**Fig 1D and Fig S1A**). Furthermore, SPT16 was enriched at BRD4 binding sites, and vice versa, suggesting that FACT and BRD4 occupy the same chromatin regions **(Fig 1E and Fig S1B)**.

In confirmation of the physical interaction between these proteins, an antibody targeting BRD4 co-immunoprecipitated both FACT subunits (SSRP1 and SPT16) in DMG nuclear extracts **(Fig 1F)**. However, BRD4 was absent in FACT IPs, which may be due to epitope masking, where the IP antibody obstructed the surface of the complex required for its interaction with BRD4, a common issue in co-IP assays [47]. FACT and BRD4 were in complex with H3K27M and H3K27ac, in agreement with previous reports by us and others demonstrating that FACT binds to H3K27M [19, 41] **(Fig 1F).** These biochemical and genomic results imply that both FACT and BRD4 bind to, and play a role in the oncogenic functioning of H3K27M in DMG. We next used CUT&RUN to further elucidate the interaction of these two proteins, finding that SPT16 and BRD4 occupied unique and overlapping genes, with 190 genes in common, which is a significant 24-fold over enrichment compared to expectations by chance (hypergeometric p-value = 7.98e-212) **(Fig 1G and Table S1A).** Genes occupied by both SPT16 and BRD4 were involved in transcription and chromatin regulation **(Fig S1C),** including the tumor stem cell master regulator *SOX2* [48], the p53 negative regulator *MDM4* [49], and the catalytic subunit of the SWI/SNF chromatin remodeling complex *SMARCA2* [50] **(Fig 1H)**.

Since DMG is heavily driven by epigenetic and transcription dysregulation, we hypothesized that FACT and BET proteins, as in other cancers [19, 20, 51-54], would be upregulated in DMG. Consistently, *SSRP1*, *SUPT16H*, and *BRD4* were overexpressed in DMG/High Grade Glioma (HGG) patients from the ZERO childhood cancer program compared to normal fetal brain (NFB) tissue [55, 56] with (fold-change 1.7 - 4.2; $p<0.0001$) **(Fig S1D).** These genes

were also upregulated (fold-change 1.5 – 2.7; $p<0.0001$) in H3K27M DMG cell lines compared to non-malignant cell lines from the Childhood Cancer Model Atlas [57] **(Fig S1E).** Furthermore, SSRP1 and BRD4 proteins were upregulated in a panel of DMG cell lines compared to normal astrocytes, with an average of 19-fold and 8-fold increase in protein expression for BRD4 and SSRP1 respectively (**Fig S1F**). In summary, FACT and BRD4 are overexpressed, interact, and co-localize at transcriptionally active chromatin, along with H3K27M, in the vicinity of key developmental genes required for DMG growth. This prompted us to test the combination of FACT and BET inhibition as a therapeutic strategy.

Combined FACT and BET inhibition synergistically decrease DMG cell proliferation

Treatment with either of the BET inhibitors JQ1 or trotabresib resulted in decreased proliferation of primary DMG cells, with 72h IC_{50} values ranging from 1-50 μM and 0.6-7 μM, respectively, across a range of DMG cultures (**Fig 2A-B and Table S2-3**). Subsequent investigation into the impact of FACT or BRD4 inhibition on DMG isogenic cell lines, with or without the H3K27M mutation, revealed significantly increased sensitivity to single-agent CBL0137, JQ1, and trotabresib in cells bearing the H3K27M mutation. Notably, significant differences were observed in both IC_{50} and area under the curve (AUC) values between wild-type and H3K27M mutant cultures, with a 5-fold increase in sensitivity observed in H3K27M mutant compared to H3K27-KO (wild-type) DMG cells for CBL0137 and JQ1, and a 4-fold increase for trotabresib treatment (**Fig 2C, Fig S2A-C and Table S4**).

Next, we assessed the effect of combined inhibition of both FACT and BRD4. We found potent efficacy of the combination of CBL0137 and JQ1/trotabresib in H3K27M mutant cell lines, with no synergy observed in the KO cells (**Fig 2D-E**). This synergistic effect of the combination therapy on cell proliferation was similarly observed in short term cytotoxicity assays across three patient-derived DMG cell cultures, SU-DIPGVI, HSJD-DIPG007, RA055, all H3K27M mutant (**Fig 2F and Fig S2D-G**). The combinations also led to synergistic inhibition of colony formation, at concentrations of each compound ranging between 25-50 nM for SU-DIPGVI, and 100-200 nM for HSJD-DIPG007 and RA055 (**Fig 2G and Fig S2H-K**). Together, these data highlight the potential of combined FACT and BRD4 targeted inhibition as an effective strategy in H3K27M mutant DMG.

Combined FACT and BET inhibition causes chromatin condensation at gene promoters in DMG.

Given that CBL0137 and BET inhibitors each target known epigenetic and transcriptional regulators [17-19, 58], we next sought to determine the effect of these drugs on chromatin structure and transcriptional regulation. To measure chromatin accessibility, ATAC-seq was performed in two H3.3 K27M DMG cell lines (HSJD-DIPG007 and SU-DIPGVI) treated with either CBL0137 or JQ1 as monotherapies or in combination after 4 hours to examine the early and direct changes to chromatin at doses previously used in other mechanistic studies [20, 29, 35, 59, 60]. Combinatorial treatment of DMG with CBL0137 and JQ1 led to a decrease in ATAC-seq signal at transcription start sites (TSSs) (**Fig 3A)**, consistently observed across independent replicates from both cell lines tested (**Fig S3A**). This effect was largely driven by CBL0137, with Principal Component Analysis (PCA) revealing that the CBL0137 treated samples clustered closely with combination treated samples (**Fig S3B**).

We next examined chromatin accessibility at DNA with SPT16 and BRD4 CUT&RUN peaks in HSJD-DIPG007 cells, finding that both drugs alone, and in combination, decreased chromatin accessibility at these genomic regions (**Fig 3B**). This suggests that FACT and BRD4 are important for maintaining open chromatin, and that inhibition of these factors with CBL0137 and JQ1 leads to chromatin closure/condensation at these sites. Further, differential accessibility analysis revealed that combination treatment resulted in ~15-fold more closed chromatin regions compared to open regions in both cell lines tested (SU-DIPGVI: 41,457 regions closed vs. 2,620 regions opened; HSJD-DIPG007: 11,704 regions closed vs. 828 regions opened, FDR<0.05, fold-change>2X) (**Fig 3C, Fig S3C-D, and Table S1B**). There was a significant degree of overlap of the regions closed by the combination treatment in both the models **(Fig 3D)** (hypergeometric p-value = 0.008). These regions were enriched at proximal gene promoters (**Fig 3E**) with their annotated genes involved in development, proliferation, and histone modification (**Fig 3F**). This indicates that combination treatment leads to chromatin condensation at the promoters of genes involved in pathways critical for DMG tumorigenesis. For example, the combination led to chromatin condensation at the promotor of *NES* (**Fig 3G**)*,* encoding the neural progenitor marker Nestin, which is essential for glioma development [61, 62]. Remarkably, combination treatment also decreased chromatin accessibility near the promoters of *SUPT16H* (SPT16) and *BRD4* – encoding the protein targets of CBL0137 and JQ1 (**Fig 3G**).

H3K27M disrupts the balance of repressive H3K27me3 and active H3K27ac histone modifications, decreasing H3K27me3 and increasing H3K27ac [8]. We have previously shown that CBL0137 can increase global H3K27me3 levels after 24h [19]. In order to assess whether the immediate and direct chromatin changes in response to drug treatment related to changes in trimethylation we next tested the effect at the shorter timepoint of 4h. Despite

evidence that FACT and BRD4 interact with H3K27M on chromatin (**Fig 1E-F**), inhibition of these factors did not consistently affect global H3K27me3 or H3K27ac levels at this early timepoint, observed through western blotting or ELISA assays (**Fig S3E-G**). Furthermore, CBL0137 treatment did not significantly alter H3K27me3 levels or distribution at individual gene loci using CUT&RUN (**Fig S3H-I**), together indicating that chromatin remodeling induced by CBL0137 is not reliant on H3K27me3 restoration within this early timeframe. These results are in line with the relatively slow turnover rates (3 days) for H3K27me3 [63].

CBL0137 and JQ1 cause widespread gene expression changes

To investigate the impact of chromatin condensation of CBL0137 and JQ1 treatment on transcription, we performed RNA-seq on matching cells from the ATAC-seq experiments. Differential gene expression analysis revealed that the combination treatment led to the largest degree of gene expression changes in both cell lines (FDR<0.05, fold-change>1.5X), with more genes becoming downregulated than upregulated (**Fig 4A and Table S1C**) when comparing each treatment to the DMSO control. Consistently, multidimensional scaling of RNA-seq samples revealed distinct clustering based on the drug treatments, with the combination treatment responsible for the most variation in gene expression between the cohorts (**Fig S4A**).

Analyses of the differentially expressed genes common to both DMG cell lines (**Fig 4B**) indicated that genes downregulated in response to combination treatment were involved in several processes critical for the sustained growth and proliferation of cancer cells, such as RNA processing (RNA modification, tRNA modification, rRNA modification), ribosome biogenesis, and DNA repair (**Fig S4B and Fig 4C**). Conversely, combination treatment led to upregulation of stress (e.g. regulation of transcription in response to stress and the unfolded protein response) and transmembrane transport pathways, reflecting an acute stress response to the drug combination (**Fig S4B and Fig 4C**).

CBL0137 and JQ1 combination treatment represses transcription of key oncogenes

We next examined the relationship between chromatin occupancy and the drug-induced alterations to chromatin accessibility and gene transcription through integration of the CUT&RUN, ATAC-seq and RNA-seq datasets. Most of genes bound by SPT16 and BRD4 had decreased expression when these proteins were simultaneously inhibited, suggesting that FACT and BRD4 directly activate a subset of the genes they occupy. This effect was primarily driven by JQ1, as the transcriptional profile of the JQ1-treated samples resembled

that of the combination-treated samples (**Fig 5A**). As expected, the majority of genes with decreased promoter accessibility upon combination treatment also had decreased transcription with each single agent, exhibiting an intermediate level of expression between that of the control and combination treatment (**Fig 5B**). Together, this indicates that dual targeting of FACT and BRD4 leads to compaction of chromatin and to transcriptional silencing at specific loci.

Among the silenced genes were several key oncogenic drivers, for example *MYC, PDGFRA* and *MDM4*. *MYC* is an established transcriptional target of both FACT and BRD4 [26, 58]. Accordingly, we found SPT16 and BRD4 to be localized to the *MYC* promoter, marked by H3K4me3 and H3K27ac histone modifications (**Fig 5C)**. Furthermore, this same region had decreased chromatin accessibility in combination-treated cells (**Fig 5C)** with a concomitant downregulation of both *MYC* mRNA (**Fig 5D and Fig S5A**) and protein expression following 24 hours (**Fig 5E and Fig S5B**). *PDGFRA* encodes another prominent super-enhancer associated glioma oncogene [35, 36]. SPT16, and BRD4 albeit to a lesser degree, were similarly localized to the *PDGFRA* promoter and putative upstream enhancer, with condensed chromatin at these loci, and repression on both the mRNA and protein level upon combination treatment (**Fig 5C-E and Fig S5A-B**). Another silenced oncogene was *MDM4*, which is a p53 negative regulator with additional p53-independent oncogenic roles [49, 64] (**Fig 5C-E and Fig S5A-B**). Interestingly, p53 protein was only upregulated by CBL0137, and only in the context of wildtype p53 HSJD-DIPG007 cells, but not in p53-mutant SU-DIPGVI cells **(Fig S5D-E)**. The same patterns of FACT/BRD4 co-localization, chromatin compaction, and decreased transcription were observed for *PTCH1,* an important member of the hedgehog signaling pathway shown to be elevated in DMG [45], and a consistent PTCH1 protein decrease was observed in SU-DIPGVI cells (**Fig S5E-G).** Finally, *LARP1, an* RNA binding protein and mTOR effector involved in ribosome biosynthesis [65], and *KLHDC8A,* a super-enhancer driven glioma oncogene involved in hedgehog signaling [66], had similar epigenetic and transcriptional repression, however, these did not manifest in a significant decrease in protein expression (**Fig S5E-G).**

CBL0137 and JQ1 alter the splicing landscape in DMG

Given the downregulation of RNA processing genes in CBL0137 and JQ1 combination-treated cells (**Fig 4C**), and the fact that chromatin is known to regulate splicing through a co-transcriptional process [67], we next examined splicing in our RNA-seq experiments. Treatment with CBL0137 or JQ1 as single agents demonstrated limited differential splicing. However, compared to control cells, combination treatment led to hundreds of differential

splicing events with an average of 800 and 2000 events in HSJD-DIPG007 and SU-DIPGVI cells, respectively (**Fig S6A**), with a proportion of these events occurring within the same gene, resulting in approximately 400 unique genes in HSJD-DIPG007 cells and 1000 unique genes in SU-DIPGVI cells (**Fig S6B and Table S1D**)**.** The most common form of alternative splicing was intron retention, equating to 40-50% of events (**Fig S6C**). Next, we investigated the potential regulation of splicing by drug-induced changes to chromatin architecture. We observed a statistically significant overlap (hypergeometric p-values = 1.64e-10 for HSJD-DIPG007 and 3.14e-56 for SU-DIPGVI) in genes which had both closed chromatin and differential splicing, equating to 81 shared genes in HSJD-DIPG007 and 430 shared genes in SU-DIPGVI cells. (**Fig S6D**). An example of intron retention is shown at *SPTBN2* (**Fig S6E**). This gene also had chromatin condensation and reduced expression (**Fig S6E-F**) and encodes for β-III spectrin which has been implicated as a driver in multiple cancer types [68-70]. Interestingly, non-coding transcripts corresponding to retained introns for this gene have been documented (**Fig S6G**) [71]. These findings indicate that epigenetic modulation with CBL0137 and JQ1 disrupts the transcriptional splicing landscape in DMG.

CBL0137 and JQ1 modulate the interferon response in DMG and in macrophages

While our earlier experiments assessed the early and direct epigenetic effects of drug treatment in DMG, we next assessed expression changes after an extended 48h treatment. In keeping with the recognized ability of CBL0137 to invoke an interferon response [72], we show that CBL0137 treatment for 48h elevated expression of interferon stimulated genes (ISGs) in HSJD-DIPG007 cells, including statistically significant increases in *IRF1*, *OAS1* and the expression of antigen presentation genes (*HLA-A, HLA-B, HLA-C)* (**Fig S7A**), whilst concomitantly increasing expression of *IFNα, IFNβ, IFNγ*, and *IL-6* (**Fig S7B**). BRD4 has been shown to play a role in the transcriptional regulation of ISGs [73]. Here, we found that inhibition of BRD4 in DMG modulates both ISGs and cytokine mRNA expression, which is largely recapitulated in DMG exposed to a combination of CBL0137 and JQ1 (**Fig S7A-B**).

Given that macrophages are the most prominent immune cell type in DMG [15], and that macrophage polarization into M1 and M2 states is epigenetically regulated [74]**,** we next assessed the ability of CBL0137 and JQ1 to modulate the inflammatory response within cultured macrophages. Compared to untreated controls, macrophages exposed to CBL0137 demonstrated significantly increased expression in the pro-inflammatory M1 macrophage markers *IL-1β, p53* and *iNOS* (**Fig S7C**) and increased expression of M2 markers *IRF3* and *HIF-1α* (**Fig S7D**). Conversely, macrophages exposed to JQ1 responded with upregulation of the M1 markers *IL-1β* and *IRF8*, with no significant increase in M2 marker expression. The

combination of CBL0137 and JQ1 resulted in the increased expression of the M1 markers *IL-1α, IL-1β, p53* and *IRF5*, whilst also increasing the M2 marker *HIF-1α*. Together, these data indicate that this combinatorial therapeutic approach has the potential to positively modulate the immune microenvironment.

Dual inhibition of FACT and BRD4 enhances survival in orthotopic models of DMG

To evaluate therapeutic efficacy, we utilized three orthotopic xenograft models using distinct patient-derived DMG cells: SU-DIPGVI-LUC, RA055, and HSJD-DIPG007. These models were chosen for their ability to faithfully replicate the diffuse infiltration characteristics observed histologically in DMG tumors.

In the SU-DIPGVI-LUC model, single-agent treatments with CBL0137 and JQ1 exhibited either negligible or limited anti-tumor effects, respectively. However, the combination regimen, which was well-tolerated with no observed weight loss, significantly extended survival compared to single-agent treatments and vehicle cohorts by delaying tumor growth, as seen by xenogen imaging (median survival: vehicle: 73 days, CBL0137: 76 days, JQ1: 78 days, CBL0137/JQ1: 95.5 days; **Fig 6A-B**, **Fig S8A** and **Table S5**). Immunohistochemical analysis of brain tissue collected following 4 weeks of combination treatment revealed a significant reduction in cell proliferation, as evidenced by decreased Ki67 staining, and a concurrent reduction in H3K27ac staining (**Fig 6C-D**).

These promising results were recapitulated in the highly aggressive RA055 model, characterized by a median survival of 46 days in untreated mice post intracranial injection. Treatment with the combination of CBL0137 and JQ1 significantly enhanced survival, with approximately one-third of treated mice surviving until the experimental endpoint of 201 days (**Fig 6E**, **Fig S8B** and **Table S6**). Consistent with the SU-DIPGVI-LUC model, cell proliferation and H3K27ac immunohistochemistry staining were significantly reduced with combination treatment compared to single-agent and untreated tissue samples (**Fig 6F and Fig S8C**). We also observed a significant reduction in MYC and MDM4 staining in PDX tumors treated with the combination, validating the *in vitro* mechanistic findings in an independent *in vivo* model.

Extension in survival with combined FACT and BRD4 inhibition was also evident in the HSJD-DIPG007 model, with the median survival of the combination-treated cohort extended to 93.5 days compared to 70.5 days in the vehicle group (**Fig S8D-E** and **Table S7**). Taken together, this combination strategy is effective against multiple aggressive DMG models.

Discussion

Despite hundreds of clinical trials, survival outcomes for DMG patients have not changed in over three decades [15]. The current standard-of-care, radiotherapy, only delays tumor progression and the majority of children still survive less than one year from diagnosis. Since the discovery of the H3K27M mutation in 2012, efforts to target multiple layers of epigenetic regulation, including DNA methylation [12], histone modification [75-78], chromatin readers [35, 36], chromatin remodelers [79-81], and transcription machinery [35, 82], have been ongoing. Due to DMG's aggressive and heterogenous nature, a monotherapy approach is unlikely to suffice. Moreover, with multiple aberrant pathways, and undruggable oncogenic drivers, even combination therapies that affect one or two pathways are unlikely to be effective. Here we have uncovered a novel mechanism-anchored epigenetic combination therapy - FACT and BET inhibition - which leads to simultaneous disruption of multiple oncogenic pathways and demonstrates potent pre-clinical activity against DMG.

FACT disassembles and reassembles nucleosomes during cellular processes that require DNA access, such as during transcription or replication. This overcomes the physical hindrance of nucleosome-compacted DNA, allowing RNA Pol II or the replication machinery to travel through chromatin unimpeded [22, 23]. Our findings indicate that FACT maintains open chromatin at promoters and enhancers, supporting transcription driven by developmental TFs (TCF12, OLIG2, SNAI1) in DMG. This parallels a recent study showing FACT's role in maintaining open chromatin at regulatory elements to promote transcription by core pluripotency TFs in embryonic stem cells [83].

BRD4 binds to acetylated chromatin via its tandem bromodomains and recruits positive transcription elongation factor (P-TEFb) to active enhancers, which releases paused RNA pol II, leading to transcriptional initiation and elongation [84]. Our findings suggest that FACT and BRD4 cooperate at promoters and enhancers to drive transcription of multiple genes vital for the growth and development of DMG, with blockade of these synergistically disrupting the transcriptional landscape, both in terms of transcript abundance and splicing. Combined targeting of FACT and BRD4 led to chromatin compaction and transcriptional silencing of several notable oncogenes. For example, *MYC, PDGFRα*, and *KLHDC8A* are all super enhancer-activated oncogenes involved in gliomagenesis [12, 66, 85]. Another downstream target was *MDM4*, a negative regulator of p53, suggesting this treatment could potentially restore p53 function in p53-WT DMGs [49]. *PTCH1* and *KLHDC8A* are both

involved in hedgehog signaling [66], which is notable given the hedgehog responsive cell-of-origin of DMG [86], and that both CBL0137 and JQ1 synergistically antagonize oncogenic hedgehog signaling in other pediatric brain cancers [87]. In sum, this drug intervention simultaneously disarms multiple epigenetic-driven oncogenes in DMG.

The combination of CBL0137 with both BET inhibitors had higher efficacy against H3K27M cells compared to isogenic cells lacking H3K27M. This could be explained by two hypotheses: i) The drugs inhibit the function of H3K27M by targeting its co-factors (FACT and BRD4), or ii) H3K27M's downstream epigenetic dysregulation sensitizes the cells to FACT and BRD4 inhibition. The former is supported by the interaction and chromatin localization between FACT and BRD4 with H3K27M, which is strengthened by an IP-mass spectrometry study identifying SPT16 and SSRP1 as binding partners of H3K27M in DMG mitotic extracts [41]. However, we did not observe marked changes in H3K27me3 levels at early timepoints after CBL0137 treatment, indicating that H3K27M's ability to inhibit PRC2 was not impacted in a short time frame. It is possible that sustained treatment is required to observe this effect, as we have previously shown that 24 hours of treatment with CBL0137 leads to increased global H3K27me3 [19]. Given the slow turnover rate of H3K27me3 (3 days) [63], extended timepoints with lower non-cytotoxic doses may be required to observe changes in H3K27me3 patterning by CUT&RUN. In the second scenario, we propose that the hypomethylated chromatin creates a dependency on FACT and BRD4 to maintain open chromatin and high levels of transcription (see graphical abstract). CBL0137 and JQ1 treatment then leads to chromatin compaction at transcription start sites, disrupting the expression of thousands of genes. This is analogous to recent studies targeting the SWI/SNF chromatin remodeling complex, where the epigenetic reprogramming characteristic of DMG creates a dependency on this complex to drive pathogenic gene expression [79-81]. Notably, CBL0137 and JQ1 were still effective, albeit to a lesser degree, against isogenic DMG cells lacking H3K27M, and have also shown synergy in other H3K27 WT pediatric brain malignancies, such as medulloblastoma and Atypical Teratoid/Rhabdoid Tumor (AT/RT) cell lines [87], indicating potential broader therapeutic applications in pediatric brain cancers beyond H3K27M DMG.

The three-dimensional (3D) organization of the genome is an additional layer of epigenetic regulation and is emerging as a critical contributor to tumorigenesis in epigenetic driven cancers such as DMG and Ependymoma [42, 88]. Both CBL0137 and BET inhibitors have known roles in targeting genome topology, disrupting topologically associating domains (TADs) and chromatin loops to alter enhancer-promoter communication [42, 60]. While this

epigenetic aspect was not addressed in this study, understanding the impact of combination treatment on 3D genome architecture represents an exciting future direction.

We uncovered a role for combination treatment in regulating mRNA splicing. As splicing is influenced by chromatin structure, we hypothesize that alternative splicing could arise due to stalled transcription as RNA pol II attempts to travel through compacted chromatin, leading to errors caused by the splicing machinery [67]. We propose a mechanism by which changes to chromatin structure induced by CBL0137 renders the cells susceptible to transcriptional disruption, which is achieved with the addition of JQ1. However, this hypothesis warrants further exploration using nascent RNA-sequencing approaches or mapping RNA pol II rate. Notably, epigenetic therapies are well known for their activation of the immune response through various mechanisms [89]. Indeed, CBL0137 has been shown to induce double stranded RNA, triggering a type I interferon response in various non-DMG cancer models, and this can occur independently of FACT [27, 72, 90]. In our study, sustained drug treatment revealed a heightened interferon response in DMG and highlights the need to use immunocompetent models in future work.

The *in vivo* efficacy of the combined FACT and BRD4 inhibition in multiple orthotopic models of DMG indicates its potential as a promising combinatorial treatment strategy. Employing an alternative dosing regimen involving an increased dose of CBL0137 (40 mg/kg) paired with a reduced dose of JQ1 (25 mg/kg) not only proved well-tolerated but also resulted in a significantly enhanced survival response in highly aggressive DMG models. This underscores the importance of exploring diverse dosing regimens for the development of combination therapies.

In summary, our study provides compelling mechanism-based evidence for a promising novel approach to treat DMG. FACT inhibitors and BET inhibitors are both presently being tested in Phase I/II clinical trials for pediatric brain tumors as single agents (PEPN2111, NCT03936465). Our results establish a strong rationale for a combination clinical trial to improve treatment options for DMG patients.

Materials and Methods

Cell culture

DMG cells were maintained as neurospheres in Tumor Stem Cell (TSM) media consisting of a 1:1 mixture of DMEM/F12 and Neurobasal medium (Invitrogen) supplemented with

Glutamax, Pyruvate, non-essential amino acids, HEPES buffer, antibiotic/antimycotic, B-27 (Invitrogen), Heparin (0.0002%), EGF (20 ng/mL), bFGF (20 ng/mL), PDGF-AA (10 ng/mL) and PDGF-BB (10 ng/mL) (StemCell Technologies). SU-DIPGXIII K27M and K27M-KO isogenic cells were maintained according to [12], adherently on flasks coated with poly-L-ornithine (0.01%) (Sigma) and laminin (10 µg/mL) (Sigma), in Neurocult NS-A proliferation media (StemCell Technologies) supplemented with heparin (0.0002%), EGF (20 ng/mL) and bFGF (10 ng/mL) (StemCell Technologies). All lines were cultured at 37°C and 5% carbon dioxide. Cells tested negative for mycoplasma contamination and were confirmed to match their original tumors by STR profiling.

Human monocyte-derived macrophages (HMDM) were a kind gift from Prof. Kerry-Anne Rye, Cardiometabolic Research Group, UNSW, following isolation and culture as previously described [91]. In polarisation studies, HMDM were either primed for 48 h with 1 µg/mL LPS and 20 ng/mL recombinant human IFNγ for the M1 phenotype, 20 ng/mL recombinant human IL-4 and 20 ng/mL recombinant human IL-13 for the M2 phenotype, or treated for 48 h with 1µM CBL0137 or 1µM JQ1, alone or in combination, and total RNA extracted, and cDNA generated for qPCR, as detailed below.

Co-immunoprecipitation (co-IP) assay

Co-IP was performed as described in [92]. Briefly, nuclei were isolated from 5 million cells with hypotonic buffer (20 mM Tris-HCl pH 7.4, 10 mM NaCl, 3 mM $MgCl_2$, protease inhibitors (Roche)) for 15 min on ice, followed by addition of IGEPAL (0.5%). Nuclei were collected by centrifugation (5 min, 1000 *x g*, 4°C) then lysed in non-denaturing lysis buffer (50mM HEPES pH 7.4, 140 mM NaCl, 3 mM $MgCl_2$, 1 mM EGTA, 1% Triton-X, 10% Glycerol, protease inhibitors (Roche)). The nuclear lysate was passed 6 times through a 25-G needle to shear the DNA, then incubated for 15 min on ice. Lysates were cleared by centrifuging at 13,000 rpm (top speed) for 15 min at 4°C to remove insoluble debris. The lysate supernatant was then incubated with 15 µL protein A/G magnetic beads (Pierce) pre-conjugated with 2.5 µg antibody (minimum 4 h, 4°C with rotation). Immunoprecipitation was carried out overnight at 4°C on a rotator. Magnetic beads were washed 3x with lysis buffer, and protein was eluted with 2X Laemmli Sample Buffer diluted in lysis buffer, boiled at 85°C for 10 min, followed by addition of DTT (100 mM). Western blotting to detect immunoprecipitated proteins was performed as described below, except that VeriBlot (Abcam) was used for the secondary antibody at 1:1000.

Western blotting

To extract total protein cells were incubated with RIPA buffer (CST) containing protease and phosphatase inhibitors (Roche) for 15 min on ice with occasional vortexing, followed by centrifugation at 13,000 rpm for 15 min at 4°C to remove debris. To extract histones, the histone extraction kit (abcam) was used according to the manufacturer's protocol. Protein concentration was determined using a BCA kit (Pierce). Protein samples (20-30 µg RIPA-soluble proteins, or 3 µg for histones) were prepared with 1X Laemmli SDS loading dye then boiled for 5 min at 95°C. BioRad 4-20% proTEAN pre-cast gels were used for gel electrophoresis, and proteins were transferred for 1 h at 100 V onto 0.45 µm PVDF membranes for RIPA-soluble proteins, or 0.45 µm nitrocellulose membranes for histones. Membranes were blocked for 1 h in 5% milk diluted in Tris Buffered Saline with 0.01% Tween-20 (TBS-T). Western blotting was carried out overnight with the indicated antibodies (Table 1) diluted 5% Bovine Serum Albumin (BSA) in TBS-T. Following washing, membranes were incubated in horseradish peroxidase- conjugated secondary antibody (CST) diluted in 5% skim milk/TBS-T (1:2000) for 1 hr at room temperature. Membranes were incubated with ECL substrate (Pierce) and bands imaged using a Bio-Rad ChemiDoc imaging system. Densitometry was carried out using Image Lab software, with local background subtraction, and normalization to the indicated housekeeping gene.

ELISA

Histone extracts were isolated as described above and 200 ng was used to analyze global H3K27me3 and H3K27ac levels using ELISA kits according to the manufacturer's protocol (EpiGenTek). Samples were run in technical duplicate wells, and the experiment repeated 3 independent times.

qPCR

Total RNA was extracted with an ISOLATE II RNA Mini Kit and first-strand cDNA generated using a SensiFAST cDNA Synthesis Kit, with quantitative real-time PCR (qRT-PCR) performed through the use of the SensiFAST SYBR No-ROX Kit (Meridian Bioscience), using specific primers sequences (Table 2), synthesized by Integrated DNA Technologies. Relative mRNA expression of genes of interest were normalized against the corresponding house-keeping genes, using the delta-delta Ct method [93].

CUT&RUN

HSJD-DIPG007 neurospheres were collected by centrifugation at 800 rpm for 3 min and dissociated into single cells with 1 mL Accutase (Sigma) for 5-10 minutes with occasional pipetting, diluted with 5 mL TSM-B, and passed through a 40 µm cell strainer. Cells were centrifuged at 1,200 rpm for 5 min and resuspended in complete media. Single cell

suspensions were counted using a haemocytometer and cell viability was confirmed to be over 95%. CUT&RUN was performed using the EpiCypher CUTANA CUT&RUN kit according to the manufacturer's instructions. Briefly, 500,000 viable cells per reaction were washed and permeabilized with 0.01% Digitonin, which was determined to be the minimum concentration for effective permeabilization. Cells were incubated with 0.5 µg antibody, or a 1:50 dilution for SPT16 (Table 1), on a nutator overnight at 4°C. Following washing, pAG-MNase was added to the reactions and $CaCl_2$ was used to activate antibody-bound MNase for targeted chromatin digestion and release of DNA fragments. The entire volume of purified DNA (ranging from 1-10 ng) was used as input for NGS library preparation, according to the EpiCypher CUTANA Library Prep Kit instructions. Library concentration was determined using a Qubit Fluorometer (HS dsDNA) (Thermo) and library size determined using a 4200 Tapestation system on a high sensitivity D1000 ScreenTape (Agilent). Resulting libraries were sequenced with 50-150bp paired-end reads, with a minimum of 7M reads per sample. Two biological CUT&RUN replicates were performed.

CUT&RUN analysis

Quality control analysis of CUT&RUN reads was performed using fastQC (v0.11.9). Adapter trimming was performed using cutadapt (v4.2) with parameters: --error-rate 0.1 --times 1 --overlap 3 --action trim --minimum-length 17 --pair-filter any. Reads were aligned using bowtie2 (v2.5.0) with -k 1 against the GRCh38 human reference genome. BAM files were sorted, and optical duplicates marked using picard (v2.27.5) with parameters: --DUPLICATE_SCORING_STRATEGY SUM_OF_BASE_QUALITIES --OPTICAL_DUPLICATE_PIXEL_DISTANCE 100 --VALIDATION_STRINGENCY SILENT. Marked duplicates were filtered and removed using samtools (v1.12). Peak calling was performed using MACS2 (v2.2.7.1) using IgG as the control. Narrow peaks parameters: --keep-dup all -p 1e-5 and broad peak using parameters: --keep-dup all -q 0.05 --broad --broad-cutoff 0.05. BigWig coverage files were generated using deeptools bamCoverage (v3.5.1) with parameters: --binSize 10 --normalizeUsing BPM --effectiveGenomeSize 2913022398. Broad peak settings were used for H3K27M and H3K27me3, and narrow peaks for SPT16, BRD4, H3K27ac, H3K4me3. Peaks from biological replicates were overlapped using BedTools [94].

BigWig coverage was visualized using DeepTools [95] at the following genomic regions: hg38 Ensembl genes, H3K27me3 CUT&RUN peaks, H3K27me3 CUT&RUN peaks, SPT16 CUT&RUN peaks and BRD4 CUT&RUN peaks (all from this study) and H3K27ac ChIP-seq peaks (GSE162976[42]), with blacklisted CUT&RUN regions excluded [96]. Integrated genomics viewer (IGV) [97] was used to visualize BigWig coverage and MACS peak calls at

individual loci. Peaks were annotated using ChIPSeeker [98] and ClusterProfiler [99] was used for Gene Ontology over-representation analysis of the annotated genes. To determine if the overlap between the SPT16 and BRD4 associated genes was significantly over-enriched a hypergeometric test was performed using the following parameters: number of successes k = 190 (overlapping genes) sample size s = 478 (BRD4 peak genes common to n=2 reps) number of successes in the population M = 1093 (SPT16 peak genes common to n=2 reps) population size N = 67,319 (number of genes in hg38), where expected = (s*M)/N. Transcription factor motif analysis was performed using the Cistrome SeqPos motif tool [100]. Differential binding analysis for H3K27me3 comparing between DMSO and CBL0137 treated cells was carried out using CSAW as described [101], filtering on genomic windows 5-fold higher than background, with a significance threshold of FDR < 0.05 (n=2).

ATAC-seq

Neurospheres were treated for 4 h with CBL0137 and JQ1 (HSJD-DIPG007 1 µM CBL0137 1 µM JQ1; SU-DIPGVI 2 µM CBL0137 1 µM JQ1). DMSO was added to the control and single drug treatments to equal concentration in all conditions (maximum 0.03% DMSO). Transposition was performed as described in the OMNI-ATAC-seq protocol [102]. Briefly, single cell suspensions from neurospheres were prepared as described for CUT&RUN and washed in ice-cold PBS and cell viability was confirmed to be over 95%. Nuclei from 50,000 viable cells were isolated, permeabilized and transposed with 2.1 µL Tn5 (Illumina) for 30 min with mixing (1000 rpm). DNA was then purified, and PCR amplified (7-14 cycles) with sequencing primers to generate libraries for sequencing. Library concentration was determined using a Qubit Fluorometers (Thermo) (HS dsDNA) and library size determined using a 4200 Tapestation system on a high sensitivity D1000 ScreenTape (Agilent). ATAC-seq libraries were sequenced with a minimum of 50 million paired-end reads per sample and read length 100bp. ATAC-seq experiments were performed in biological duplicate (HSJD-DIPG007) or triplicate (SU-DIPGVI).

ATAC-seq analysis

ATAC-seq reads were trimmed with Trimmomatic (ILLUMINACLIP:Nextera.fa:2:30:10:8:TRUE SLIDINGWINDOW:5:20 LEADING:3 TRAILING:3 MINLEN:20 CROP:130 HEADCROP:150). Trimmed reads were mapped with bowtie2 using default settings [103] and the resulting BAM files deduplicated using Sambamba markdup [104]. Deduplicated BAM files were then filtered to remove reads with fragment sizes greater than 100bp and CPM BigWigs were generated using the DeepTools bamCoverage [95].

BigWig coverage was visualized as heatmaps and profile plots using DeepTools [95] at the following genomic regions: hg38 Ensembl genes, H3K27me3 CUT&RUN peaks, H3K27ac ChIP-seq peaks, H3K27me3 CUT&RUN peaks, SPT16 CUT&RUN peaks and BRD4 CUT&RUN peaks (all from this study, except for H3K27ac from GSE162976[42]). PCA clustering of ATAC-seq average signal over gene bodies was performed using DeepTools. Differential accessibility analysis was carried out using CSAW as described [101], filtering on genomic windows 5-fold higher than background. Regions with an FDR<0.05 were considered significantly different, with 'opened' regions logFC > 1 and 'closed' regions logFC < -1. Closed regions between the 2 models were overlapped using BedTools [94], annotated using ChIPSeeker [98] and ClusterProfiler was used for Gene Ontology over-representation analysis of the annotated genes [99]. BigWig coverage was visualized at individual gene loci on IGV [97]. A hypergeometric test was used to test if the overlap in 'closed regions' between the 2 models was significantly over-enriched (k = 6119 (overlap), s = 11704 (closed in HSJD-DIPG007), M = 41,454 (closed in SU-DIPGXIII), N = 80,894 (number of windows analyzed), where expected = (s*M)/N.

RNA-seq

Neurospheres were treated with CBL0137 and JQ1 for 4 h and collected for both ATAC-seq and RNA-extraction. Total RNA was extracted from treated cells using the ISOLATE II RNA Mini Kit from Meridian Bioscience. RNA concentration and purity was determined using a NanoDrop Spectrophotometer and integrity measured using a 4200 Tapestation system. cDNA libraries were prepared using the Illumina Stranded mRNA prep kit. RNA-seq libraries were sequenced with 100bp paired-end reads, with a minimum of 50 million reads per sample. Three biological replicates were performed for all RNA-seq experiments.

RNA-seq analysis

Illumina paired-end fastq files were aligned to the human genome GRCh38 and gencode v41 using STAR (v2.7.8a) in two-pass mode with quantMode set to TranscriptomeSAM [105]. Transcriptome alignment was quantified using RSEM (v1.3.3) rsem-calculate-expression to obtain raw read counts, and normalized transcripts per million (TPM) and fragments per kilobase million (FPKM) values [106]. Degust (10.5281/zenodo.3258932) was used for differential expression analysis, using edgeR for normalization. Genes with low expression were filtered out using a cutoff of 0.5 counts per million (CPM) in at least 3 samples. Genes with FDR<0.05 and absolute logFC>0.585 (1.5-fold) were considered significantly differentially expressed. Multi-dimensional Scaling (MDS) clustering was performed using Degust. ClusterProfiler was used for Gene Ontology over-representation analysis of the differentially expressed genes [99]. A hypergeometric test was used to

determine the over enrichment of the overlapping up or downregulated genes between the 2 models (k = number of overlapping genes, s = number of genes in HSJD-DIPG007 model, M = number of genes in HSJD-DIPG007 model, N = 20,000 coding genes in human genome), where expected = (s*M)/N.

MINTIE [107] was used for differential splicing analysis using parameters assembler=soap, min_logfc=2, min_cpm=0.1, fdr=0.05, and run_de_step=TRUE, with all 3 Vehicle replicates used as control. BedTools [94] was used to determine the common events between the 3 biological replicates. BAM files were visualized on IGV [97] ensuring the same scale. A hypergeometric test was used to test if the overlap in closed regions and differentially spliced regions was over enriched (k = overlap, s = differentially spliced, M = closed regions, population size N = 67319 (number of genes in hg38), where expected = (s*M)/N.

Gene expression analysis from patient samples and cell lines

Patient expression data for *SSRP1, SUPT16H* and *BRD4* was obtained from the ZERO childhood cancer precision medicine program that had RNA-seq from 84 DMG/HGG patients [55]. Patient expression data were also obtained from McGill University (11 normal fetal brain samples) [56]. *SSRP1, SUPT16H* and *BRD4* expression in DMG and non-malignant cell lines was downloaded from the Childhood Cancer Model Atlas [57].

Cell Viability Assays

Cells were cultured in 96-well plates at a density of 2,500-3,000 cells per well in a final volume of 0.2 mL of cell culture media. The cells were subjected to specific treatments as indicated in the study. Adherent cells had the drugs added 24 hours after plating, while suspension cells received the drugs 72 hours after plating. After an incubation period of 72 hours, cell proliferation was evaluated using the resazurin assay (Sigma-Aldrich). The resulting data was expressed as a percentage relative to the untreated cells.

Clonogenic Assays

Long-term clonogenic assays were conducted by plating 24-well plates with a base layer of 0.3 mL of 0.5% agar mixed with cell culture media. After 24 hours of incubation at 4°C, the base layer was overlaid with a 0.4 mL layer consisting of cells (500-1500 cells/well), 0.33% agar, cell culture media, and the drug at the indicated concentrations. The plates were then incubated in a 5% CO2 humidified atmosphere at 37°C. Following an incubation period of either 2 or 4 weeks, depending on the specific cell line, the colonies were stained with 3-(4,5-dimethylthiazol-2-yl)-2,5-diphenyltetrazolium bromide (MTT) solution at 5 mg/mL After 1 hour, images of the colonies were captured using Image Lab Software. Colony quantification

was performed using Image J software, and the data were presented as a percentage relative to untreated colonies.

Orthotopic model/drug treatment

The protocol for intracranial injections was implemented as described in the study conducted by Khan et al. [108]. The timing of treatment initiation varied for each model with SU-DIPGVI-Luc at 7 weeks, RA055 at 3 weeks. and HSJD-DIPG007 starting at 5 weeks post intracranial surgery.

In the SU-DIPGVI-Luc and RA055 models, the drug treatments were as follows: CBL0137 - dissolved in 5% dextrose, CBL0137 was administered intravenously at a dosage of 40 mg/kg/day. The treatment was given once every four days for a total of four weeks. JQ1 - dissolved in DMSO and subsequently in a solution containing 0.9% saline with 5% PEG400 and 5% TWEEN-80, JQ1 was administered at a dosage of 25 mg/kg/day intraperitoneally. The treatment was given five days a week over a period of four weeks.

In the HSJD-DIPG007 model, the drug treatments included: CBL0137 - dissolved in 5% dextrose, CBL0137 was administered intravenously at a dosage of 20 mg/kg/day. The treatment was given five days a week for a total of four weeks. JQ1 - Dissolved in DMSO and subsequently in a solution containing 0.9% saline with 5% PEG400 and 5% TWEEN-80, JQ1 was administered intraperitoneally at a dosage of 50 mg/kg/day. The treatment was given five days a week for a duration of four weeks.

Throughout the study, the survival of the mice was closely monitored daily. Neurological and clinical symptoms were assessed to detect signs of tumor development. Mice exhibiting clinical signs of neurological decline, such as ataxia, circling, head tilting, with or without a 20% weight loss, were humanely euthanized. All animal experiments strictly adhered to the guidelines set by the Animal Care and Ethics Committee of the University of New South Wales and the Australian Code of Practice for the Care and Use of Animals for Scientific Purposes. The experimental protocols used in this study were approved under protocol number 22/46B.

Histological analysis of brain tissue

Brain samples were collected on the final day of treatment and fixed in a 10% formalin neutral buffered solution obtained from Sigma-Aldrich. The fixed samples were then embedded in paraffin wax, and 5-mm sections were cut and mounted on glass slides. To prepare the sections for histological examination, dehydration was carried out.

Subsequently, the sections were stained with hematoxylin/eosin and Ki67, H3K27ac, MDM4, and MYC (Table 1) using the BOND RX Fully Automated Research Stainer (Leica biosystems) for histologic examination. Following staining, positive cells were identified and quantified using Andy's Algorithms [109] on the image analysis pipeline on FIJI.

Table 1. List of antibodies

Target	Catalogue number	Application
SSRP1	CST 1341	WB
SSRP1	Biolegend 609710	IP
SPT16	CST 12191	WB, CUT&RUN
SPT16	Biolegend 607002	IP
BRD4	CST 13340	IP, WB
BRD4	EpiCypher 13-2003	CUT&RUN
ß-Actin	CST 8457	WB
IgG rabbit	EpiCypher 13-0042	CUT&RUN
IgG mouse	Santa Cruz 2025	IP
H3K4me3	EpiCypher 13-0041	CUT&RUN
H3K27me3	CST 9733	CUT&RUN, WB
H3K27ac	CST 8173	CUT&RUN, WB
H3K27ac	Abcam ab4729	IHC
H3K27M	CST 74829	CUT&RUN, WB
Histone H3	CST 9717	WB
C-MYC	CST 18583	WB
C-MYC	Abcam 32072	IHC
PDGFRα	CST 3164	WB
MDM4	BETHYL-A300-287	WB
MDM4	Abcam 244366	IHC
P53	CST 2527	WB
PTCH1	CST 2468	WB

LARP1	CST 14763	WB
KLHD8CA	nbp1-31181	WB
Ki67	Thermofisher RM-9106 SP6	IHC

Table 2. Sequences of qPCR primers

Gene	Forward	Reverse	GenBank
18s	GAGGATGAGGTGGAACGTGT	TCTTCAGTCGCTCCAGGTCT	NM_022551.2
Arg1	GTCTGTGGGAAAAGCAAGCG	TTGCCAAACTGTGGTCTCCG	NM_001244438.1
B2M	AGATGAGTATGCCTGCCGTG	GCGGCATCTTCAAACCTCCA	NM_004048.2
CD86	ACTAGCACAGACACACGGATG	CTTCAGAGGAGCAGCACCAGAG	NM_175862.4
CD206	CACGATCCGACCCTTCCTTG	GTCTCCGCTTCATGCCATTG	NM_002438.3
Egr2	TTTGTGCACCAGCTGTCTGA	TTGATCATGCCATCTCCGGC	NM_000399.5
FN-1	ACAAACACTAATGTTAATTGCCCA	CCTCCAGAGCAAAGGGCTTA	NM_212482.2
HIF1α	CTTTCCTTCTCTTCTCCGCGT	TTTCGACGTTCAGAACTTATCTTTT	NM_001530.4
HLA-A	CACAGACTGACCGAGTGGAC	GGATGGTGTGAGAACCGGC	NM_002116.8
HLA-B	GCAGTTGTGGTCATCGGAGC	TCCCTCCTTTTCCACCTGAACT	NM_005514.8
IFNα	ACTCATACACCAGGTCACGC	TGGTCATAGTTATAGCAGGGGTG	NM_024013.2
IFNβ	GCGACACTGTTCGTGTTGTC	GAGCTGTAGTGGAGAAGCACA	NM_002176.4
IFNγ	GAGTGTGGAGACCATCAAGGA	TGGACATTCAAGTCAGTTACCGAA	NM_000619
IL-1β	CAGGCTGCTCTGGGATTCTC	GTCCTGGAAGGAGCACTTCAT	NM_000576
IL-6	CCAGAGCTGTGCAGATGAGT	AGCTGCGCAGAATGAGATGA	M54894.1
IL-8	TCTGCAGCTCTGTGTGAAGG	TTCTCCACAACCCTCTGCAC	NM_000584.3
IL-29	CCCCCAAAAAGGAGTCCGC	CTCAGACACAGGTTCCCATCG	NM_172140.2
iNOS	CTGGCAAGCCCAAGGTCTAT	TCCCCGCAAACATAGAGGTG	NM_000625.4
IRF1	TCTTCCCTCTTCCACTCGGA	TGATGGGCATGTTGGCTCTG	NM_002198.3
IRF3	GACCTTCCATCGTAGGCCG	CTCTTGTTCACCCAGGCCAC	NM_001571.6
IRF5	GAAAGCGAGCTCGGACCC	GGTACTGGCAGCTGTTCACC	NM_032643.5
IRF7	TGTGCTGGCGAGAAGGC	TGGAGTCCAGCATGTGTGTG	NM_001572.5
IRF8	CAAACTAGGCGTGGCAACTG	AATCGTCCACAGAAGGCTCC	NM_001363907.1
MCP-1	AGCCACCTTCATTCCCCAAG	TTGGGTTTGCTTGTCCAGGT	X14768.1
OAS1	CTGGCACAAGAGGCTGAGG	CACTGTTGCTTTCAGCCAGC	NM_016816.4
OAS3	TGAACAAGGCCGTTGATACC	GCTGAAGAGCCACCCTTGA	NM_006187.4
p53	GTTCCGAGAGCTGAATGAGG	TCTGAGTCAGGCCCTTCTGT	AF098067

SOCS1	CACTTCCGCACATTCCGTTC	CAGTAGAATCCGCAGGCGTC	NM_003745.2
TNFα	CCCATGTTGTAGCAAACCCTC	TATCTCTCAGCTCCACGCCA	NM_000594.3

Data Availability

Raw and processed NGS data is currently being uploaded onto the GEO repository.

Main figure legends

Figure 1. FACT and BRD4 expression and co-localization in DMG

A) Genomic distribution of SPT16 peaks (1,095 peaks common to 2 replicates) compared to a background of ~1000 randomly shuffled genomic regions. **B)** Dot plot of over-represented gene ontologies for genes associated with SPT16 peaks. **C)** Transcription factor motif enrichment analysis and motif logos for SPT16 peaks. **D)** Heatmaps depicting SPT16, BRD4, H3K27M and IgG CUT&RUN signal (red) and ATAC-seq signal (blue) at transcription start sites, H3K4me3 promoter peaks, H3K27ac enhancer peaks (from [42]) and H3K27me3 heterochromatin peaks in HSJD-DIPG007 neurospheres. Heatmaps are ranked based on ATAC-seq signal. Representative data from n=2 experiments. **E)** Profile plots depicting the average SPT16 and BRD4 signal at SPT16 peaks (left) and BRD4 peaks (right) in HSJD-DIPG007 cells. Representative data from n=2 experiments. **F)** Co-Immunoprecipitation and western blotting in HSJD-DIPG007 nuclear extracts showing direct interactions between BRD4 with the FACT subunits, H3K27M and H3K27ac. Representative data from n=3 experiments. **G)** Venn diagram depicting overlapping annotated genes from 2 independent SPT16 and BRD4 CUT&RUN replicates. A hypergeometric test was used to determine over enrichment. **H)** Gene tracks display input, SPT16 and BRD4 CUT&RUN signal at promoters of developmental and cancer-related genes *SOX2, MDM4* and *SMARCA2.* Bars beneath coverage tracks represent MACS2 peak calls.

Figure 2. Combinatorial FACT and BRD4 inhibition decreases cell proliferation and colony formation in H3K27M mutant DMG cells.

Patient-derived DMG cell lines are sensitive to BRD4 inhibition via **A)** JQ1 and **B)** trotabresib. **C)** Sensitivity to FACT and BRD4 inhibitors, CBL0137 and JQ1 and trotabresib respectively, was significantly higher in isogenic SU-DIPGXIII H3K27M cells compared to KO cells. Combination treatment of **D)** CBL0137 and JQ1 and **E)** CBL0137 and trotabresib was synergistically effective in isogenic SU-DIPGXIII H3K27M cells, with no efficacy observed in KO cells. SU-DIPGVI cells have, upon combined FACT and BRD4 inhibition, synergistically decreased **F)** cell survival and **G)** form fewer colonies. Data is presented as

mean values ± SEM of three independent experiments. **p<0.01, ***p<0.001, ****p<0.0001. P-values were calculated by **C)** two-tailed t-tests for H3K27M and H3K27M-KO cells and **G)** 2-way ANOVA for single and combination treatments. Combination index values were calculated by Calusyn.

Figure 3. CBL0137 and JQ1 condense chromatin at gene promoters.

A) Heatmaps depicting ATAC-seq signal at transcription start sites in HSJD-DIPG007 (left) and SU-DIPGVI (right) cells treated with DMSO, CBL0137 (1µM for HSJD-DIPG007 and 2µM for SU-DIPGVI), JQ1 (1µM) or the combination for 4 hours. Average signal is shown in the profile plots above. Representative data from n=2 experiments for HSJD-DIPG007 and n=3 experiments for SU-DIPGVI. **B)** Profile plots depicting the average ATAC-seq signal at SPT16 peaks (top) and BRD4 peaks (bottom) in HSJD-DIPG007 cells with the indicated treatments. **C)** Volcano plot showing differentially accessible regions in HSJD-DIPG007 cells. Blue data points represent significantly (FDR < 0.05, fold-change < -2) downregulated "closed" regions, red data points represent significantly upregulated "opened" (FDR < 0.05, fold-change > 2) regions, with the number of regions indicated. **D)** Venn diagram displaying the overlap between the closed regions common to both cell lines. A hypergeometric test was used to determine over enrichment. **E)** Genomic distribution of the overlapping closed regions from panel D compared to background ATAC-seq regions. **F)** Dot plot of over-represented gene ontologies in the genes associated with the overlap regions from panel D. **G)** Gene tracks display ATAC-seq signal near promoters *NES*, *SUPT16H,* and *BRD4* in HSJD-DIPG007 (upper) and SU-DIPGVI (lower) with the indicated treatments. Representative replicate from n=2-3 experiments.

Figure 4. CBL0137 and JQ1 cause widespread gene expression changes

A) Volcano plots depicting the significantly differentially expressed genes in HSJD-DIPG007 cells (upper panels) and SU-DIPGVI cells (lower panels) treated with DMSO, CBL0137 (1µM for HSJD-DIPG007 and 2µM for SU-DIPGVI), JQ1 (1µM) or the combination for 4 hours. Blue data points represent significantly (FDR < 0.05, fold-change < -1.5) downregulated genes, red data points represent significantly upregulated genes (FDR < 0.05, fold-change > 1.5), with the number of genes indicated. **B)** Venn diagrams displaying the intersecting downregulated (blue) and upregulated (red) genes in combination-treated cells compared to DMSO between the 2 DMG models. A hypergeometric test was used to determine over enrichment. **C)** Enrichment map of over-represented gene ontologies in the up (left) and downregulated (right) genes from the overlap regions from panel B.

Figure 5. Chromatin compaction by CBL0137 and JQ1 decreases expression of oncogenes

A) Heatmaps depicting Z-scores for RNA-seq TPM values across the 4 indicated treatments at genes associated with SPT16 and BRD4 peaks in HSJD-DIPG007 cells **B)** Heatmaps depicting Z-scores for RNA-seq TPM values across the 4 indicated treatments at genes associated with promoters (<1kb from TSS) with decreased accessibility in combination treated HSJD-DIPG007 cells (logFC < -1.5, left) and SU-DIPGVI cells (logFC< -2.5 right) (n=3). **C)** Gene tracks displaying H3K27ac ChIP-seq [42], H3K4me3, IgG, SPT16, BRD4 CUT&RUN (CR), and ATAC-seq signal across the 4 indicated treatments in HSJD-DIPG007 and SU-DIPGVI cells at the *MYC*, *PDGFRA* and *MDM4* loci. These promoters and putative enhancers are occupied by SPT16 and BRD4 and decrease in accessibility in combination treated cells. **D)** Bar charts displaying RNA-seq TPM values (mean +/- SEM; n=3) for *MYC*, *PDGFRA* and *MDM4* in HSJD-DIPG007 cells treated for 4h with CBL0137 (1µM) and JQ1 (1µM). **E)** Representative MYC, PDGFRα and MDM4 western blots and bar charts displaying densitometry (mean +/- SEM; n=3) normalised to the indicated housekeeper (β-Actin or α-Tubulin) and expressed as a fold-change relative to the DMSO control. Cells were treated for 24h. An ordinary one-way ANOVA with Sidak's multiple comparisons test was used to test for significance between DMSO and each treatment, and the combination treatment compared to each monotherapy.

Figure 6. Therapeutic efficacy of CBL0137 and JQ1 combination treatment in orthotopic models of DMG.

Mice were intracranially injected with DMG cells and 3-7 weeks post injection, treatments commenced. Mice were humanely euthanized when they displayed severe neurological decline and/or weight loss or reached maximum holding time (MHT). **A)** Survival curve of SU-DIPGVI-Luciferase with CBL0137/JQ1 treatment. Median survival of cohorts (days): Vehicle (n=9) = 73, CBL0137 (n=9) = 76, JQ1 (n=6) = 78, CBL0137 + JQ1 (n=6) = 95.5. Exact p-values listed in Supplementary Table 5. **B)** Xenogen imaging showed the effect of CBL0137/JQ1 on SU-DIPGVI-Luciferase tumors. Immunohistochemistry staining for **C)** Ki67 and **D)** H3K27ac of DMG tumors post 4 weeks of treatment in SU-DIPGVI-Luciferase model. Three images were taken from brain samples collected from three mice in each cohort. Scale: 50µm . **E)** Survival curve of RA055 orthotopic model with CBL0137/JQ1 treatment. Median survival of cohorts (days): Vehicle (n=12) = 46, CBL0137 (n=9) = 51, JQ1 (n=8) = 55, CBL0137 + JQ1 (n=9) = 66. Exact p-values listed in Supplementary Table 6. Immunohistochemistry staining for **F)** Ki67, **G)** MYC and **H)** MDM4 of DMG tumors in the RA055 model. Three images were taken from brain samples collected from three mice in each cohort at the end of the treatment period. Scale: 50µm. **A, E)** Shaded areas indicate

treatment period of combination treatment in each model. Statistical analysis has been performed using the Log-Rank (Mantel-Cox) with multiple test corrections applied. **C,D,F,G,H)** Data is presented as mean values ± SEM. *p<0.05, **p<0.01, ***p<0.001, ****p<0.0001. p-values were calculated using one-way ANOVA for treated and untreated cohorts.

Supplementary Table 1: Gene lists identified in CUT&RUN, ATAC-seq and RNA-seq experiments.

A) Genes associated with SPT16 and BRD4 MACS2 peaks from two independent CUT&RUN experiments in HSJD-DIPG007 cells. Genes from individual replicates, combined replicates, and overlapping genes between SPT16 and BRD4 combined replicates are listed. **B)** Unique genes associated with ATAC-seq CSAW differentially accessible regions (DAR) with FDR<0.05 and fold-change >2x = opened, fold-change < -2x = closed in HSJD-DIPG007 and SU-DIPGVI cells treated with CBL0137 (1µM HSJD-DIPG007 and 2µM SU-DIPGVI) and JQ1 (1µM) for 4h. **C)** RNA-seq significantly differentially expression genes with FDR<0.05 and fold-change >1.5x = UP, fold-change < -1.5x = DOWN in HSJD-DIPG007 and SU-DIPGVI cells treated with CBL0137 (1µM HSJD-DIPG007 and 2µM SU-DIPGVI) and JQ1 (1µM) for 4h. **D)** Genes with differential splicing common to 3 independent replicates in HSJD-DIPG007 and SU-DIPGVI treated with CBL0137 (1µM HSJD-DIPG007 and 2µM SU-DIPGVI) and JQ1 (1µM) in combination for 4h.

Acknowledgments

We would like to express our gratitude to Michelle Monje, Angel Montero Carcaboso, and Esther Hulleman for their generous provision of the SU-DIPG, HSJD-DIPG, and VUMC-DIPG10 cells, respectively, which were instrumental in the success of this study. We thank Nada Jabado and Brian Krug for providing the isogenic H3K27M KO SU-DIPGXIII models and Yunjia Zhang, Oluwaseyi Samson Ogunmodede, and Kerry-Anne Rye for providing the HMDM cells. We also acknowledge the Core Services Group at Children's Cancer Institute for their valuable technical support throughout the research. We extend our appreciation to the Flow Cytometry Core Facility, BRIL Facility, and BMSF Facility (Russel Pickford) at UNSW assistance in flow cytometry, imaging, and pharmacokinetic testing, respectively, which greatly contributed to our data analysis and interpretation. We also acknowledge the Garvan Institute Histopathology Facility for their services. Furthermore, we would like to acknowledge the Zero Childhood Cancer Program and the Tumour Bank teams at CCI for their significant contributions to the establishment of primary DIPG and normal astrocyte

cultures, which were indispensable for our investigations. The authors thank the Children's Cancer Institute Animal Facility for providing support to this study. We would like to thank Nathan Dahl and Lays Sobral for technical advice regarding CUT&RUN and ATAC-seq. This work has generously been funded by the Kids Cancer Alliance, We Love You Connie Foundation Grant, Levi's Project, CINSW Fellowship (HH) (2022/ECF1425), The Kids Cancer Project Col Reynolds Fellowship (AK), NHMRC Synergy Grant (2019056), Cancer Institute NSW Translational Program Grant (2019/TPG2037), NHMRC Investigator grant (GNT2017898), and DIPG Collaborative: The Cure Starts Now (2018). Graphical abstract created with BioRender.com.

Author Contributions

Conceptualization: MT, DSZ. **Methodology:** HH, AK, JL. **Formal Analysis:** HH, AK, AE, NJ, SER, XG, HN, CM, BR. **Investigation:** HH, AK, AE, AG, HN, AL, BR, MT. **Data Curation:** HH, AK, CM, XG, NJ, SER. **Visualization:** HH, AK, SER, YCS, BR. **Writing – Original Draft:** HH, AK. **Writing – Review & Editing:** All. **Supervision:** CM, BR, MT, MD, DSZ. **Project Administration:** HH, AK. **Funding Acquisition:** HH, BR, MT, DSZ.

Declaration of Interests

DSZ declares consulting/advisory board fees from Bayer, Astra Zeneca, Accendatech, Novartis, Day One, FivePhusion, Amgen, Alexion, and Norgine and research support from Accendatech. The remaining authors have declared that no competing interests exist.

References

1. Louis, D.N., et al., *The 2021 WHO Classification of Tumors of the Central Nervous System: a summary.* Neuro-Oncology, 2021. **23**(8): p. 1231-1251.
2. Schwartzentruber, J., et al., *Driver mutations in histone H3.3 and chromatin remodelling genes in paediatric glioblastoma.* Nature, 2012. **482**(7384): p. 226-231.
3. Khuong-Quang, D.A., et al., *K27M mutation in histone H3.3 defines clinically and biologically distinct subgroups of pediatric diffuse intrinsic pontine gliomas.* Acta Neuropathol, 2012. **124**(3): p. 439-47.
4. Wu, G., et al., *Somatic histone H3 alterations in pediatric diffuse intrinsic pontine gliomas and non-brainstem glioblastomas.* Nat Genet, 2012. **44**(3): p. 251-3.
5. Castel, D., et al., *Histone H3 wild-type DIPG/DMG overexpressing EZHIP extend the spectrum diffuse midline gliomas with PRC2 inhibition beyond H3-K27M mutation.* Acta Neuropathologica, 2020. **139**(6): p. 1109-1113.

6. Pratt, D., et al., *Diffuse intrinsic pontine glioma-like tumor with EZHIP expression and molecular features of PFA ependymoma.* Acta Neuropathologica Communications, 2020. **8**(1): p. 37.
7. Ajuyah, P., et al., *Histone H3-wild type diffuse midline gliomas with H3K27me3 loss are a distinct entity with exclusive EGFR or ACVR1 mutation and differential methylation of homeobox genes.* Sci Rep, 2023. **13**(1): p. 3775.
8. Lewis, P.W., et al., *Inhibition of PRC2 activity by a gain-of-function H3 mutation found in pediatric glioblastoma.* Science, 2013. **340**(6134): p. 857-61.
9. Piunti, A., et al., *CATACOMB: An endogenous inducible gene that antagonizes H3K27 methylation activity of Polycomb repressive complex 2 via an H3K27M-like mechanism.* Science Advances, 2019. **5**(7): p. eaax2887.
10. Bender, S., et al., *Reduced H3K27me3 and DNA hypomethylation are major drivers of gene expression in K27M mutant pediatric high-grade gliomas.* Cancer Cell, 2013. **24**(5): p. 660-72.
11. Harutyunyan, A.S., et al., *H3K27M induces defective chromatin spread of PRC2-mediated repressive H3K27me2/me3 and is essential for glioma tumorigenesis.* Nature Communications, 2019. **10**(1): p. 1262.
12. Krug, B., et al., *Pervasive H3K27 Acetylation Leads to ERV Expression and a Therapeutic Vulnerability in H3K27M Gliomas.* Cancer cell, 2019. **35**(5): p. 782-797.e8.
13. Nagaraja, S., et al., *Histone Variant and Cell Context Determine H3K27M Reprogramming of the Enhancer Landscape and Oncogenic State.* Mol Cell, 2019. **76**(6): p. 965-980.e12.
14. Brien, G.L., et al., *Simultaneous disruption of PRC2 and enhancer function underlies histone H3.3-K27M oncogenic activity in human hindbrain neural stem cells.* Nature Genetics, 2021.
15. Hayden, E., et al., *Therapeutic Targets in Diffuse Midline Gliomas-An Emerging Landscape.* Cancers (Basel), 2021. **13**(24).
16. Groves, A. and T.M. Cooney, *Epigenetic programming of pediatric high-grade glioma: Pushing beyond proof of concept to clinical benefit.* Front Cell Dev Biol, 2022. **10**: p. 1089898.
17. Orphanides, G., et al., *FACT, a factor that facilitates transcript elongation through nucleosomes.* Cell, 1998. **92**(1): p. 105-16.
18. Orphanides, G., et al., *The chromatin-specific transcription elongation factor FACT comprises human SPT16 and SSRP1 proteins.* Nature, 1999. **400**(6741): p. 284-8.
19. Ehteda, A., et al., *Dual targeting of the epigenome via FACT complex and histone deacetylase is a potent treatment strategy for DIPG.* Cell Rep, 2021. **35**(2): p. 108994.
20. Garcia, H., et al., *Facilitates Chromatin Transcription Complex Is an "Accelerator" of Tumor Transformation and Potential Marker and Target of Aggressive Cancers.* Cell Reports, 2013. **4**(1): p. 159-173.
21. Gurova, K., et al., *Structure and function of the histone chaperone FACT - Resolving FACTual issues.* Biochimica et biophysica acta. Gene regulatory mechanisms, 2018: p. S1874-9399(18)30159-7.
22. Safina, A., et al., *FACT is a sensor of DNA torsional stress in eukaryotic cells.* Nucleic Acids Res, 2017. **45**(4): p. 1925-1945.
23. Chang, H.-W., et al., *Mechanism of FACT removal from transcribed genes by anticancer drugs curaxins.* Science advances, 2018. **4**(11): p. eaav2131-eaav2131.
24. Neefjes, J., et al., *Chromatin as an old and new anticancer target.* Trends Cancer, 2024.
25. Gasparian, A.V., et al., *Curaxins: anticancer compounds that simultaneously suppress NF-κB and activate p53 by targeting FACT.* Science translational medicine, 2011. **3**(95): p. 95ra74-95ra74.
26. Carter, D.R., et al., *Therapeutic targeting of the MYC signal by inhibition of histone chaperone FACT in neuroblastoma.* Sci Transl Med, 2015. **7**(312): p. 312ra176.

27. Xiao, L., et al., *Dual targeting of chromatin stability by the curaxin CBL0137 and histone deacetylase inhibitor panobinostat shows significant preclinical efficacy in neuroblastoma.* Clin Cancer Res, 2021.
28. Tallman, M.M., et al., *The small molecule drug CBL0137 increases the level of DNA damage and the efficacy of radiotherapy for glioblastoma.* Cancer Letters, 2021. **499**: p. 232-242.
29. Wang, J., et al., *Effective inhibition of MYC-amplified group 3 medulloblastoma by FACT-targeted curaxin drug CBL0137.* Cell Death Dis, 2020. **11**(12): p. 1029.
30. Monje, M., et al., *Phase I trial of panobinostat in children with diffuse intrinsic pontine glioma: A report from the Pediatric Brain Tumor Consortium (PBTC-047).* Neuro Oncol, 2023. **25**(12): p. 2262-2272.
31. Bradner, J.E., D. Hnisz, and R.A. Young, *Transcriptional Addiction in Cancer.* Cell, 2017. **168**(4): p. 629-643.
32. Shi, J. and C.R. Vakoc, *The mechanisms behind the therapeutic activity of BET bromodomain inhibition.* Molecular cell, 2014. **54**(5): p. 728-736.
33. Lovén, J., et al., *Selective inhibition of tumor oncogenes by disruption of super-enhancers.* Cell, 2013. **153**(2): p. 320-34.
34. Taylor, I.C., et al., *Disrupting NOTCH Slows Diffuse Intrinsic Pontine Glioma Growth, Enhances Radiation Sensitivity, and Shows Combinatorial Efficacy With Bromodomain Inhibition.* J Neuropathol Exp Neurol, 2015. **74**(8): p. 778-90.
35. Nagaraja, S., et al., *Transcriptional Dependencies in Diffuse Intrinsic Pontine Glioma.* Cancer cell, 2017. **31**(5): p. 635-652.e6.
36. Piunti, A., et al., *Therapeutic targeting of polycomb and BET bromodomain proteins in diffuse intrinsic pontine gliomas.* Nature Medicine, 2017. **23**(4): p. 493-500.
37. Zhang, Y., et al., *Combination of EZH2 inhibitor and BET inhibitor for treatment of diffuse intrinsic pontine glioma.* Cell Biosci, 2017. **7**: p. 56.
38. Wiese, M., et al., *Combined treatment with CBP and BET inhibitors reverses inadvertent activation of detrimental super enhancer programs in DIPG cells.* Cell Death & Disease, 2020. **11**(8): p. 673.
39. Watanabe, J., et al., *BET bromodomain inhibition potentiates radiosensitivity in models of H3K27-altered diffuse midline glioma.* J Clin Invest, 2024.
40. Groves, A., J. Clymer, and M.G. Filbin, *Bromodomain and Extra-Terminal Protein Inhibitors: Biologic Insights and Therapeutic Potential in Pediatric Brain Tumors.* Pharmaceuticals, 2022. **15**(6): p. 665.
41. Bočkaj, I., et al., *The H3.3K27M oncohistone affects replication stress outcome and provokes genomic instability in pediatric glioma.* PLoS genetics, 2021. **17**(11): p. e1009868-e1009868.
42. Wang, J., et al., *Epigenomic landscape and 3D genome structure in pediatric high-grade glioma.* Science Advances, 2021. **7**(23): p. eabg4126.
43. Yu, Y., et al., *Olig2 targets chromatin remodelers to enhancers to initiate oligodendrocyte differentiation.* Cell, 2013. **152**(1-2): p. 248-61.
44. Han, S.P., et al., *SNAI1 is involved in the proliferation and migration of glioblastoma cells.* Cell Mol Neurobiol, 2011. **31**(3): p. 489-96.
45. Meel, M.H., et al., *Signaling pathways and mesenchymal transition in pediatric high-grade glioma.* Cell Mol Life Sci, 2018. **75**(5): p. 871-887.
46. Furth, N., et al., *H3-K27M-mutant nucleosomes interact with MLL1 to shape the glioma epigenetic landscape.* Cell Rep, 2022. **39**(7): p. 110836.
47. Falsone, S.F., B. Gesslbauer, and A.J. Kungl, *Coimmunoprecipitation and proteomic analyses.* Methods Mol Biol, 2008. **439**: p. 291-308.
48. Weina, K. and J. Utikal, *SOX2 and cancer: current research and its implications in the clinic.* Clin Transl Med, 2014. **3**: p. 19.
49. Marine, J.C. and A.G. Jochemsen, *MDMX (MDM4), a Promising Target for p53 Reactivation Therapy and Beyond.* Cold Spring Harb Perspect Med, 2016. **6**(7).

50. Centore, R.C., et al., *Mammalian SWI/SNF Chromatin Remodeling Complexes: Emerging Mechanisms and Therapeutic Strategies.* Trends Genet, 2020. **36**(12): p. 936-950.
51. Hsieh, F.-K., et al., *FACT in Cell Differentiation and Carcinogenesis.* Oncotarget, 2011. **2**(11): p. 830-832.
52. Sui, S., et al., *Ferritinophagy is required for the induction of ferroptosis by the bromodomain protein BRD4 inhibitor (+)-JQ1 in cancer cells.* Cell Death & Disease, 2019. **10**(5): p. 331.
53. Lu, L., et al., *Inhibition of BRD4 suppresses the malignancy of breast cancer cells via regulation of Snail.* Cell Death & Differentiation, 2020. **27**(1): p. 255-268.
54. Boyson, S.P., et al., *Functional Roles of Bromodomain Proteins in Cancer.* Cancers (Basel), 2021. **13**(14).
55. Wong, M., et al., *Whole genome, transcriptome and methylome profiling enhances actionable target discovery in high-risk pediatric cancer.* Nature Medicine, 2020. **26**(11): p. 1742-1753.
56. Jessa, S., et al., *Stalled developmental programs at the root of pediatric brain tumors.* Nature genetics, 2019. **51**(12): p. 1702-1713.
57. Sun, C.X., et al., *Generation and multi-dimensional profiling of a childhood cancer cell line atlas defines new therapeutic opportunities.* Cancer Cell, 2023. **41**(4): p. 660-677.e7.
58. Delmore, Jake E., et al., *BET Bromodomain Inhibition as a Therapeutic Strategy to Target c-Myc.* Cell, 2011. **146**(6): p. 904-917.
59. Nesher, E., et al., *Role of Chromatin Damage and Chromatin Trapping of FACT in Mediating the Anticancer Cytotoxicity of DNA-Binding Small-Molecule Drugs.* Cancer Res, 2018. **78**(6): p. 1431-1443.
60. Kantidze, O.L., et al., *The anti-cancer drugs curaxins target spatial genome organization.* Nat Commun, 2019. **10**(1): p. 1441.
61. Krupkova, O., Jr., et al., *Nestin expression in human tumors and tumor cell lines.* Neoplasma, 2010. **57**(4): p. 291-8.
62. Wang, Q., et al., *Nestin Is Required for Spindle Assembly and Cell-Cycle Progression in Glioblastoma Cells.* Mol Cancer Res, 2021. **19**(10): p. 1651-1665.
63. Zee, B.M., et al., *In vivo residue-specific histone methylation dynamics.* J Biol Chem, 2010. **285**(5): p. 3341-50.
64. Wohlberedt, K., et al., *Mdm4 supports DNA replication in a p53-independent fashion.* Oncogene, 2020. **39**(25): p. 4828-4843.
65. Tcherkezian, J., et al., *Proteomic analysis of cap-dependent translation identifies LARP1 as a key regulator of 5'TOP mRNA translation.* Genes Dev, 2014. **28**(4): p. 357-71.
66. Lee, D., et al., *Superenhancer activation of KLHDC8A drives glioma ciliation and hedgehog signaling.* J Clin Invest, 2023. **133**(2).
67. Alló, M., et al., *Chromatin and alternative splicing.* Cold Spring Harb Symp Quant Biol, 2010. **75**: p. 103-11.
68. Zhou, X., et al., *SPTBN2 Promotes the Progression of Thyroid Cancer by Accelerating G1/S Transition and Inhibiting Apoptosis.* Dis Markers, 2022. **2022**: p. 2562595.
69. Wu, C., et al., *SPTBN2, a New Biomarker of Lung Adenocarcinoma.* Front Oncol, 2021. **11**: p. 754290.
70. Yang, L. and Y. Gu, *SPTBN2 regulates endometroid ovarian cancer cell proliferation, invasion and migration via ITGB4-mediated focal adhesion and ECM receptor signalling pathway.* Exp Ther Med, 2023. **25**(6): p. 277.
71. Harrison, P.W., et al., *Ensembl 2024.* Nucleic Acids Research, 2023. **52**(D1): p. D891-D899.
72. Leonova, K., et al., *TRAIN (Transcription of Repeats Activates INterferon) in response to chromatin destabilization induced by small molecules in mammalian cells.* Elife, 2018. **7**.

73. Bachu, M., A. Dey, and K. Ozato, *Chromatin Landscape of the IRF Genes and Role of the Epigenetic Reader BRD4.* J Interferon Cytokine Res, 2016. **36**(7): p. 470-5.
74. Yang, X., et al., *Epigenetic regulation of macrophage polarization by DNA methyltransferase 3b.* Mol Endocrinol, 2014. **28**(4): p. 565-74.
75. Hashizume, R., et al., *Pharmacologic inhibition of histone demethylation as a therapy for pediatric brainstem glioma.* Nat Med, 2014. **20**(12): p. 1394-6.
76. Mohammad, F., et al., *EZH2 is a potential therapeutic target for H3K27M-mutant pediatric gliomas.* Nature Medicine, 2017. **23**(4): p. 483-492.
77. Grasso, C.S., et al., *Functionally defined therapeutic targets in diffuse intrinsic pontine glioma.* Nature Medicine, 2015. **21**(6): p. 555-559.
78. Balakrishnan, I., et al., *Senescence Induced by BMI1 Inhibition Is a Therapeutic Vulnerability in H3K27M-Mutant DIPG.* Cell Rep, 2020. **33**(3): p. 108286.
79. Mo, Y., et al., *Epigenome programing by H3.3K27M mutation creates a dependence of pediatric glioma on SMARCA4.* Cancer Discov, 2022.
80. Panditharatna, E., et al., *BAF complex maintains glioma stem cells in pediatric H3K27M-glioma.* Cancer Discov, 2022.
81. Mota, M., et al., *Targeting SWI/SNF ATPases in H3.3K27M diffuse intrinsic pontine gliomas.* Proc Natl Acad Sci U S A, 2023. **120**(18): p. e2221175120.
82. Dahl, N.A., et al., *Super Elongation Complex as a Targetable Dependency in Diffuse Midline Glioma.* Cell Rep, 2020. **31**(1): p. 107485.
83. Klein, D.C., et al., *FACT regulates pluripotency through proximal and distal regulation of gene expression in murine embryonic stem cells.* BMC Biol, 2023. **21**(1): p. 167.
84. Jang, M.K., et al., *The bromodomain protein Brd4 is a positive regulatory component of P-TEFb and stimulates RNA polymerase II-dependent transcription.* Mol Cell, 2005. **19**(4): p. 523-34.
85. Rahme, G.J., et al., *Modeling epigenetic lesions that cause gliomas.* Cell, 2023. **186**(17): p. 3674-3685.e14.
86. Monje, M., et al., *Hedgehog-responsive candidate cell of origin for diffuse intrinsic pontine glioma.* Proc Natl Acad Sci U S A, 2011. **108**(11): p. 4453-8.
87. Mo, J., et al., *Inhibition of the FACT Complex Targets Aberrant Hedgehog Signaling and Overcomes Resistance to Smoothened Antagonists.* Cancer Research, 2021. **81**(11): p. 3105.
88. Okonechnikov, K., et al., *3D genome mapping identifies subgroup-specific chromosome conformations and tumor-dependency genes in ependymoma.* Nat Commun, 2023. **14**(1): p. 2300.
89. Jones, P.A., et al., *Epigenetic therapy in immune-oncology.* Nat Rev Cancer, 2019. **19**(3): p. 151-161.
90. Somers, K., et al., *Potent antileukemic activity of curaxin CBL0137 against MLL-rearranged leukemia.* Int J Cancer, 2020. **146**(7): p. 1902-1916.
91. Rayner, B.S., et al., *Role of hypochlorous acid (HOCl) and other inflammatory mediators in the induction of macrophage extracellular trap formation.* Free Radic Biol Med, 2018. **129**: p. 25-34.
92. Holliday, H., et al., *Inhibitor of Differentiation 4 (ID4) represses mammary myoepithelial differentiation via inhibition of HEB.* iScience, 2021. **24**(2): p. 102072.
93. Livak, K.J. and T.D. Schmittgen, *Analysis of Relative Gene Expression Data Using Real-Time Quantitative PCR and the 2−ΔΔCT Method.* Methods, 2001. **25**(4): p. 402-408.
94. Quinlan, A.R. and I.M. Hall, *BEDTools: a flexible suite of utilities for comparing genomic features.* Bioinformatics, 2010. **26**(6): p. 841-2.
95. Ramírez, F., et al., *deepTools: a flexible platform for exploring deep-sequencing data.* Nucleic Acids Res, 2014. **42**(Web Server issue): p. W187-91.
96. Nordin, A., et al., *The CUT&RUN suspect list of problematic regions of the genome.* Genome Biol, 2023. **24**(1): p. 185.
97. Robinson, J.T., et al., *Integrative genomics viewer.* Nat Biotechnol, 2011. **29**(1): p. 24-6.

98. Yu, G., L.G. Wang, and Q.Y. He, *ChIPseeker: an R/Bioconductor package for ChIP peak annotation, comparison and visualization.* Bioinformatics, 2015. **31**(14): p. 2382-3.
99. Yu, G., et al., *clusterProfiler: an R package for comparing biological themes among gene clusters.* Omics, 2012. **16**(5): p. 284-7.
100. Liu, T., et al., *Cistrome: an integrative platform for transcriptional regulation studies.* Genome Biol, 2011. **12**(8): p. R83.
101. Lun, A.T. and G.K. Smyth, *csaw: a Bioconductor package for differential binding analysis of ChIP-seq data using sliding windows.* Nucleic Acids Res, 2016. **44**(5): p. e45.
102. Corces, M.R., et al., *An improved ATAC-seq protocol reduces background and enables interrogation of frozen tissues.* Nat Methods, 2017. **14**(10): p. 959-962.
103. Langmead, B. and S.L. Salzberg, *Fast gapped-read alignment with Bowtie 2.* Nat Methods, 2012. **9**(4): p. 357-9.
104. Tarasov, A., et al., *Sambamba: fast processing of NGS alignment formats.* Bioinformatics, 2015. **31**(12): p. 2032-4.
105. Dobin, A., et al., *STAR: ultrafast universal RNA-seq aligner.* Bioinformatics, 2013. **29**(1): p. 15-21.
106. Li, B. and C.N. Dewey, *RSEM: accurate transcript quantification from RNA-Seq data with or without a reference genome.* BMC Bioinformatics, 2011. **12**: p. 323.
107. Cmero, M., et al., *MINTIE: identifying novel structural and splice variants in transcriptomes using RNA-seq data.* Genome Biol, 2021. **22**(1): p. 296.
108. Khan, A., et al., *Dual targeting of polyamine synthesis and uptake in diffuse intrinsic pontine gliomas.* Nat Commun, 2021. **12**(1): p. 971.
109. Law, A.M.K., et al., *Andy's Algorithms: new automated digital image analysis pipelines for FIJI.* Sci Rep, 2017. **7**(1): p. 15717.

Diffuse Midline Glioma H3K27M mutant

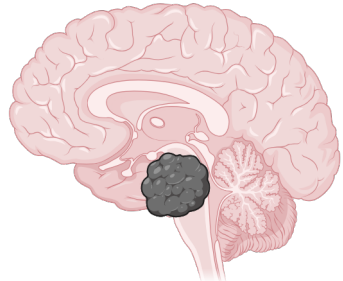

FACT and BRD4 support transcriptionally active chromatin in H3K27M DMG

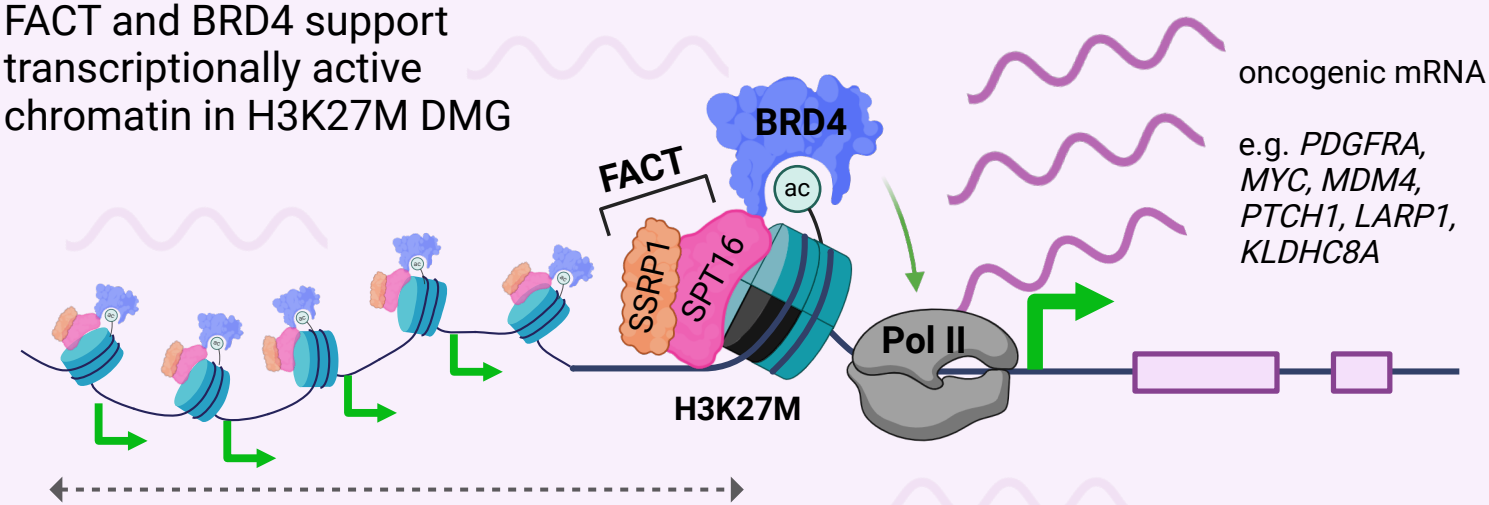

Combined inhibition leads to chromatin condensation and perturbed transcription

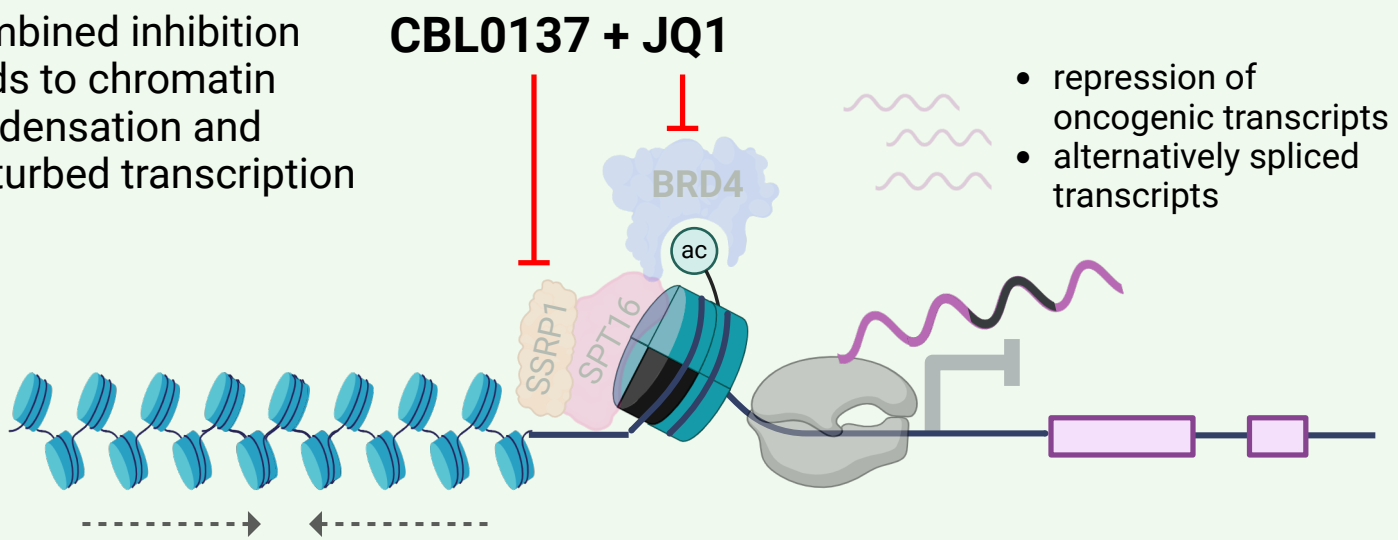

created with BioRender.com

Figure 1

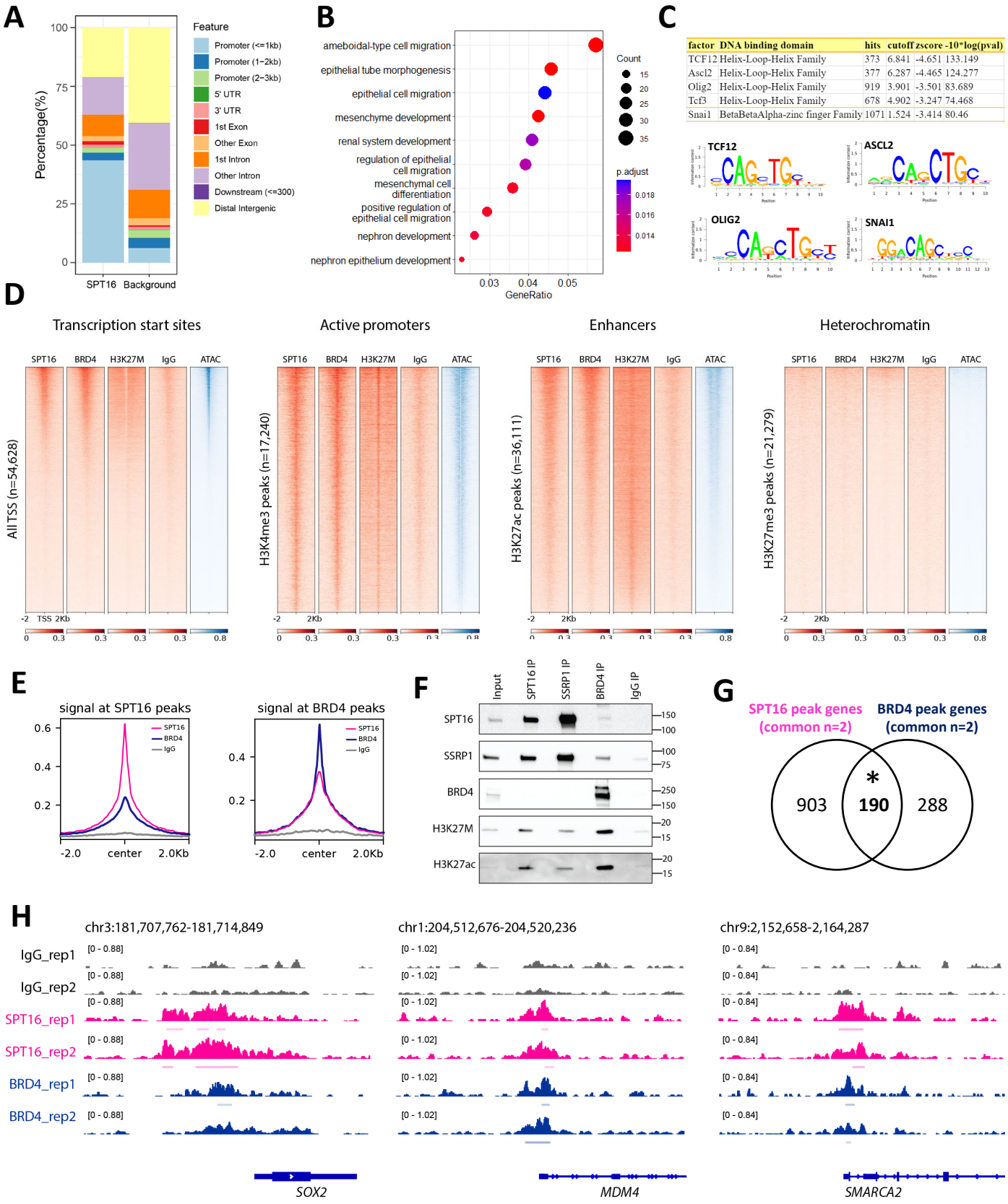

factor	DNA binding domain	hits	cutoff	zscore	-10*log(pval)
TCF12	Helix-Loop-Helix Family	373	6.841	-4.651	133.149
Ascl2	Helix-Loop-Helix Family	377	6.287	-4.465	124.277
Olig2	Helix-Loop-Helix Family	919	3.901	-3.501	83.689
Tcf3	Helix-Loop-Helix Family	678	4.902	-3.247	74.468
Snai1	BetaBetaAlpha-zinc finger Family	1071	1.524	-3.414	80.46

Figure 2

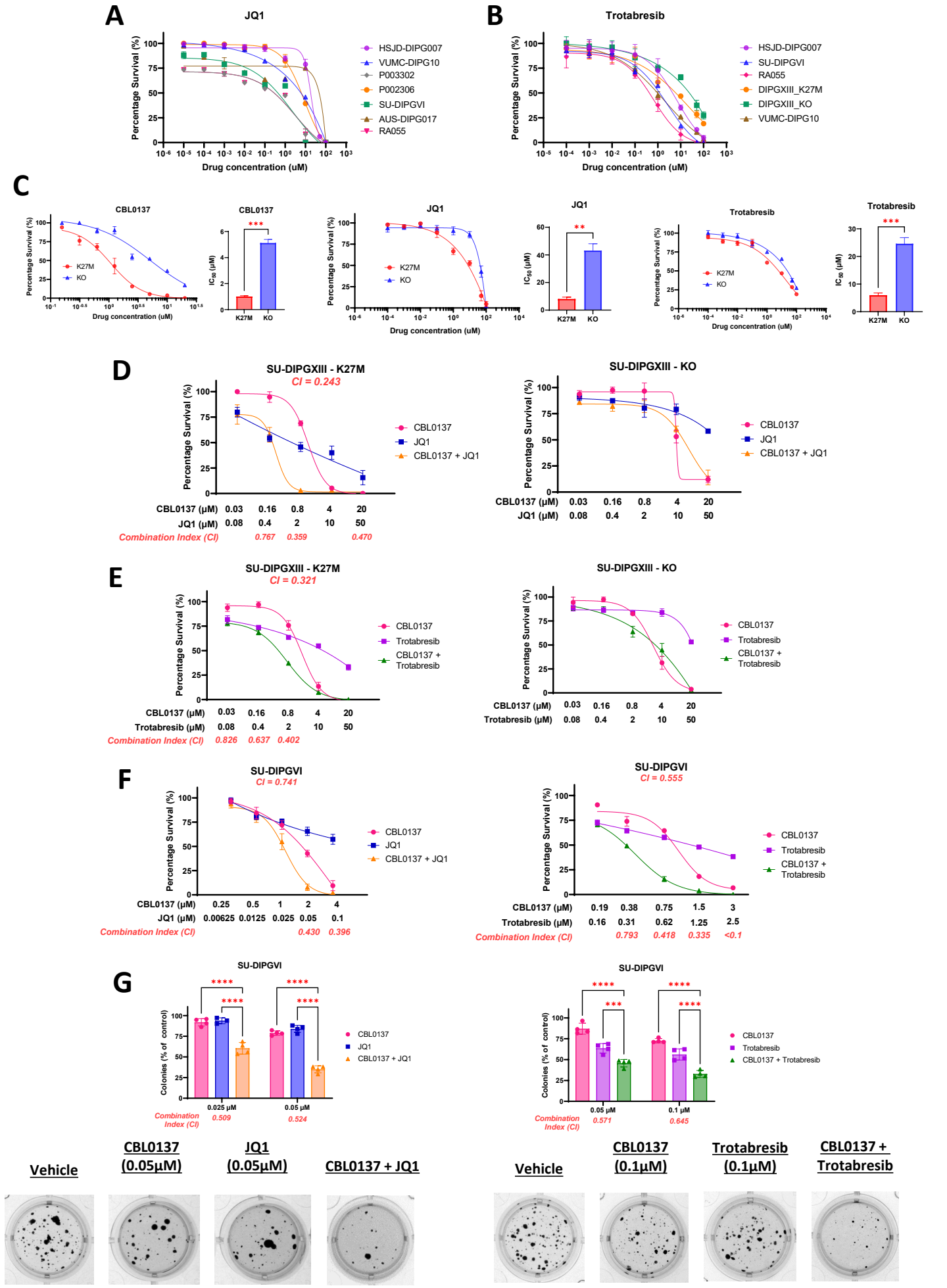
A
JQ1
Percentage Survival (%)
Drug concentration (uM)
HSJD-DIPG007
VUMC-DIPG10
P003302
P002306
SU-DIPGVI
AUS-DIPG017
RA055
B
Trotabresib
HSJD-DIPG007
SU-DIPGVI
RA055
DIPGXIII_K27M
DIPGXIII_KO
VUMC-DIPG10
C
CBL0137
K27M
KO
IC50 (µM)
JQ1
Trotabresib
D
SU-DIPGXIII - K27M
CI = 0.243
CBL0137
JQ1
CBL0137 + JQ1
CBL0137 (µM) 0.03 0.16 0.8 4 20
JQ1 (µM) 0.08 0.4 2 10 50
Combination Index (CI) 0.767 0.359 0.470
SU-DIPGXIII - KO
E
SU-DIPGXIII - K27M
CI = 0.321
Trotabresib
CBL0137 + Trotabresib
Trotabresib (µM) 0.08 0.4 2 10 50
Combination Index (CI) 0.826 0.637 0.402
SU-DIPGXIII - KO
F
SU-DIPGVI
CI = 0.741
CBL0137 (µM) 0.25 0.5 1 2 4
JQ1 (µM) 0.00625 0.0125 0.025 0.05 0.1
Combination Index (CI) 0.430 0.396
CI = 0.555
CBL0137 (µM) 0.19 0.38 0.75 1.5 3
Trotabresib (µM) 0.16 0.31 0.62 1.25 2.5
Combination Index (CI) 0.793 0.418 0.335 <0.1
G
Colonies (% of control)
0.025 µM
0.05 µM
Combination Index (CI) 0.509 0.524
0.1 µM
0.571 0.645
Vehicle
CBL0137 (0.05µM)
JQ1 (0.05µM)
CBL0137 + JQ1
CBL0137 (0.1µM)
Trotabresib (0.1µM)
CBL0137 + Trotabresib

Figure 3

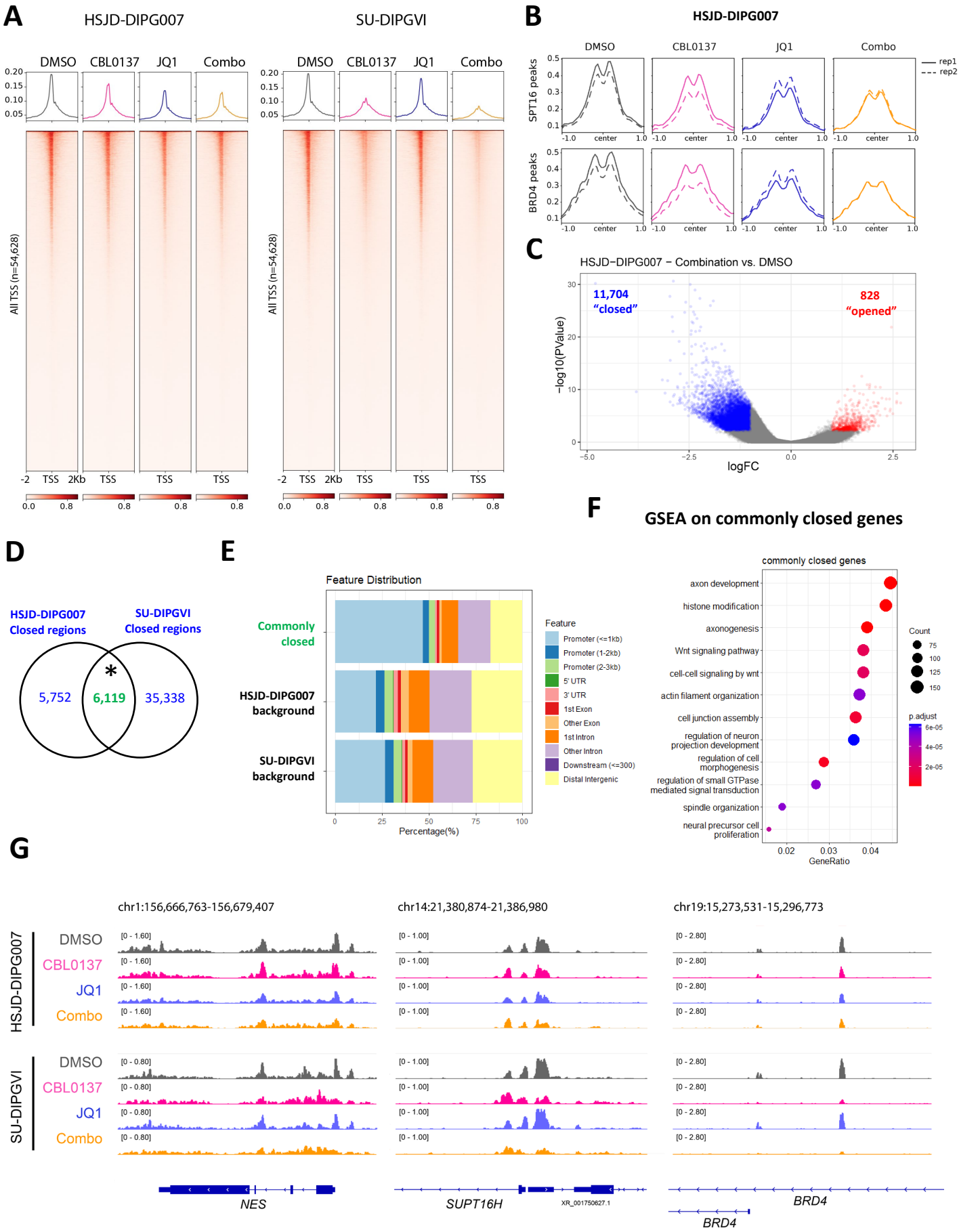
A
HSJD-DIPG007
SU-DIPGVI
DMSO
CBL0137
JQ1
Combo
All TSS (n=54,628)
-2
TSS
2Kb
B
HSJD-DIPG007
SPT16 peaks
BRD4 peaks
rep1
rep2
center
C
HSJD−DIPG007 − Combination vs. DMSO
11,704
"closed"
828
"opened"
−log10(PValue)
logFC
D
HSJD-DIPG007
Closed regions
SU-DIPGVI
Closed regions
5,752
6,119
35,338
E
Feature Distribution
Commonly closed
HSJD-DIPG007 background
SU-DIPGVI background
Percentage(%)
Feature
Promoter (<=1kb)
Promoter (1-2kb)
Promoter (2-3kb)
5' UTR
3' UTR
1st Exon
Other Exon
1st Intron
Other Intron
Downstream (<=300)
Distal Intergenic
F
GSEA on commonly closed genes
commonly closed genes
axon development
histone modification
axonogenesis
Wnt signaling pathway
cell-cell signaling by wnt
actin filament organization
cell junction assembly
regulation of neuron projection development
regulation of cell morphogenesis
regulation of small GTPase mediated signal transduction
spindle organization
neural precursor cell proliferation
GeneRatio
Count
p.adjust
G
chr1:156,666,763-156,679,407
chr14:21,380,874-21,386,980
chr19:15,273,531-15,296,773
HSJD-DIPG007
SU-DIPGVI
NES
SUPT16H
XR_001750627.1
BRD4

Figure 4

A

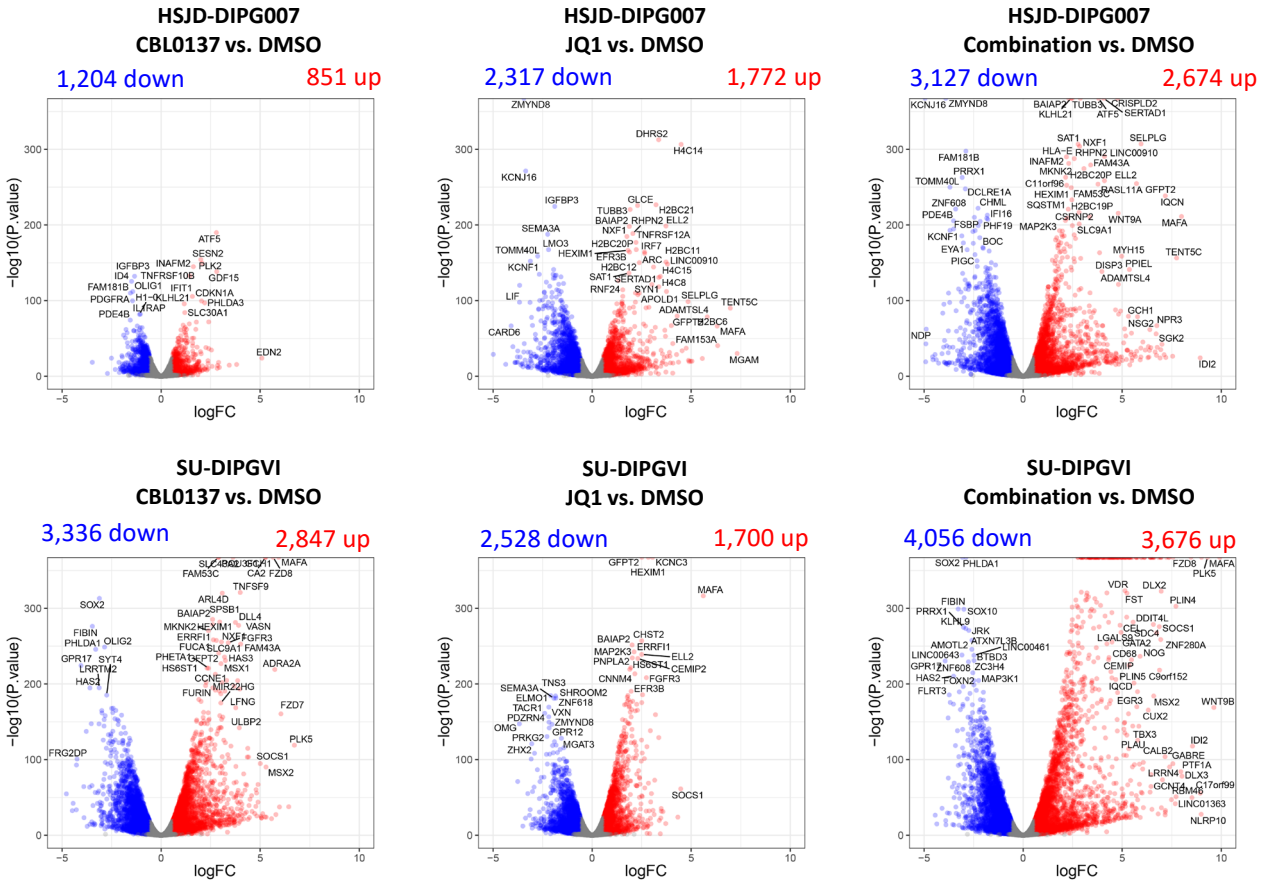

B

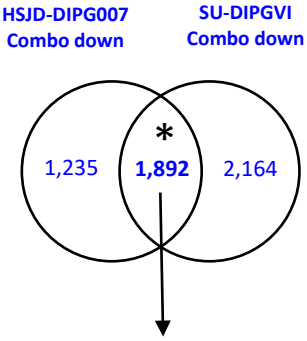

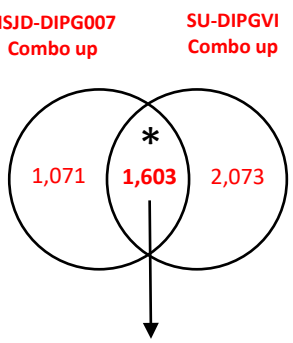

C

Common downregulated Combination vs. DMSO

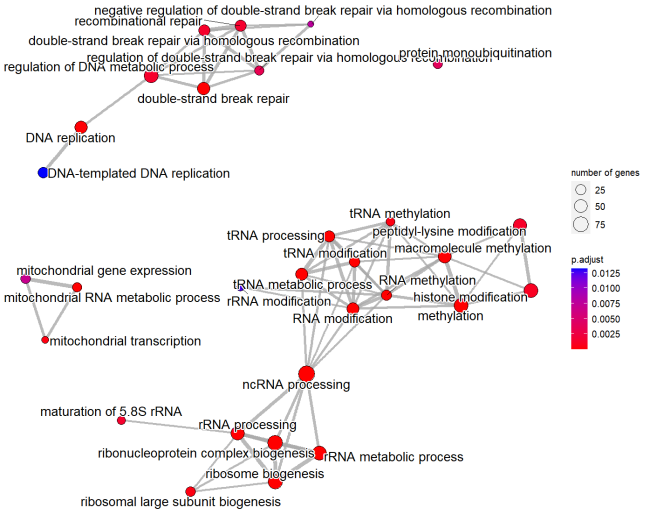

Common upregulated Combination vs. DMSO

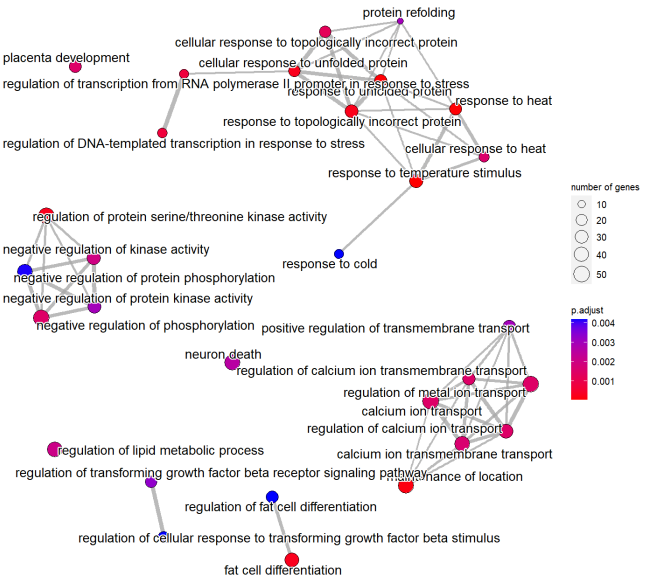

Figure 5

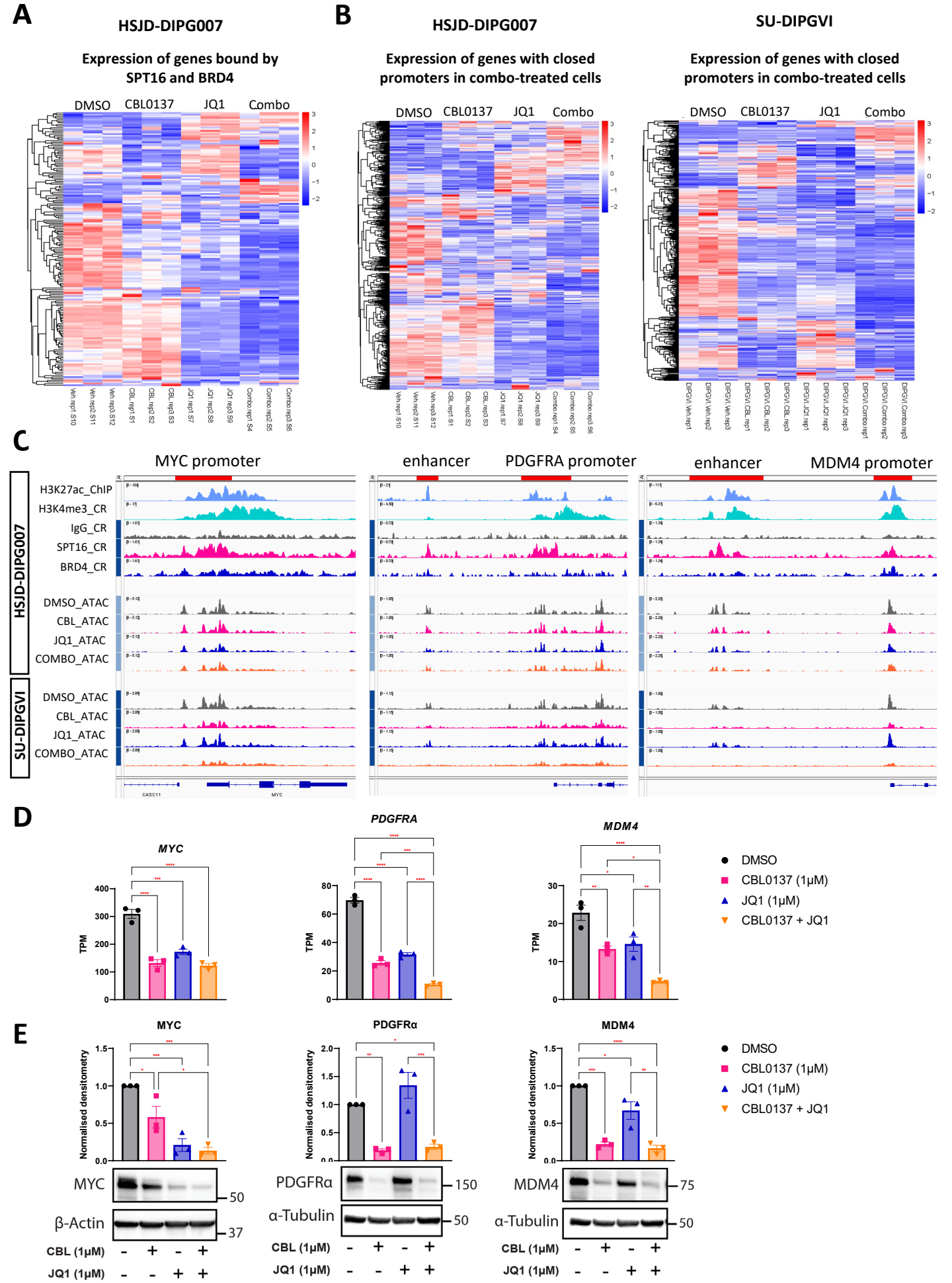
A
HSJD-DIPG007
Expression of genes bound by SPT16 and BRD4
DMSO
CBL0137
JQ1
Combo
B
HSJD-DIPG007
Expression of genes with closed promoters in combo-treated cells
SU-DIPGVI
Expression of genes with closed promoters in combo-treated cells
C
MYC promoter
enhancer
PDGFRA promoter
enhancer
MDM4 promoter
HSJD-DIPG007
H3K27ac_ChIP
H3K4me3_CR
IgG_CR
SPT16_CR
BRD4_CR
DMSO_ATAC
CBL_ATAC
JQ1_ATAC
COMBO_ATAC
SU-DIPGVI
DMSO_ATAC
CBL_ATAC
JQ1_ATAC
COMBO_ATAC
D
MYC
PDGFRA
MDM4
TPM
DMSO
CBL0137 (1μM)
JQ1 (1μM)
CBL0137 + JQ1
E
MYC
PDGFRα
MDM4
Normalised densitometry
MYC
β-Actin
PDGFRα
α-Tubulin
MDM4
α-Tubulin
CBL (1μM)
JQ1 (1μM)

Figure 6

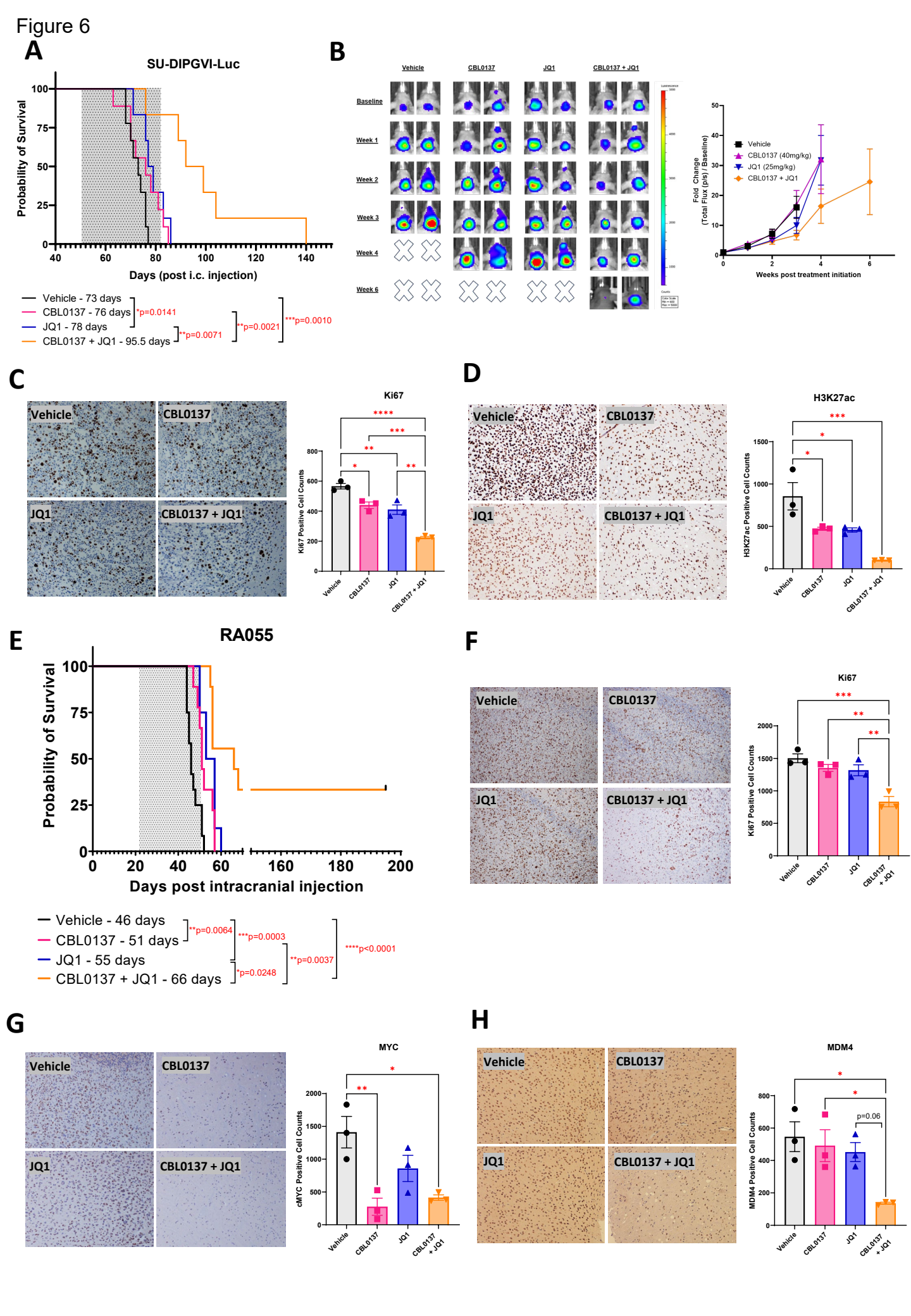
A
SU-DIPGVI-Luc
Probability of Survival
Days (post i.c. injection)
Vehicle - 73 days
CBL0137 - 76 days
JQ1 - 78 days
CBL0137 + JQ1 - 95.5 days
*p=0.0141
**p=0.0071
**p=0.0021
***p=0.0010
B
Vehicle
CBL0137
JQ1
CBL0137 + JQ1
Baseline
Week 1
Week 2
Week 3
Week 4
Week 6
Fold Change (Total Flux (p/s) / Baseline)
Vehicle
CBL0137 (40mg/kg)
JQ1 (25mg/kg)
CBL0137 + JQ1
Weeks post treatment initiation
C
Vehicle
CBL0137
JQ1
CBL0137 + JQ1
Ki67
Ki67 Positive Cell Counts
D
Vehicle
CBL0137
JQ1
CBL0137 + JQ1
H3K27ac
H3K27ac Positive Cell Counts
E
RA055
Probability of Survival
Days post intracranial injection
Vehicle - 46 days
CBL0137 - 51 days
JQ1 - 55 days
CBL0137 + JQ1 - 66 days
**p=0.0064
***p=0.0003
*p=0.0248
**p=0.0037
****p<0.0001
F
Vehicle
CBL0137
JQ1
CBL0137 + JQ1
Ki67
Ki67 Positive Cell Counts
G
Vehicle
CBL0137
JQ1
CBL0137 + JQ1
MYC
cMYC Positive Cell Counts
H
Vehicle
CBL0137
JQ1
CBL0137 + JQ1
MDM4
MDM4 Positive Cell Counts
p=0.06